Supporting information to Live imaging of silver nanostructures electrochemically dissolving at open-circuit potential

Andreas Körner*[, a, b, **], A. Lucía Morales*[, a, b, **], Birk Fritsch[a], Lena Fiedler[a, b], Justin T. Mulvey[c], Christian Göllner[a], Damien Alloyeaue, Joseph P. Patterson[c, d], Paolo Malgaretti[a], Karl J.J. Mayrhofer[a, b], Serhiy Cherevko[a], Andreas Hutzler[a, **]

[a] Forschungszentrum Jülich GmbH, Helmholtz Institute Erlangen-Nürnberg for Renewable Energy (IET-2), Cauerstr. 1, 91058 Erlangen, Germany

[b] Friedrich-Alexander-Universität Erlangen-Nürnberg, Department of Chemical and Biological Engineering, Immerwahrstr. 2a, 91058 Erlangen, Germany

[c] Department of Material Science and Engineering, University of California−Irvine, Irvine, California 92697, United States

[d] Department of Chemistry, University of California−Irvine, Irvine, California 92697, United States

[e] Laboratoire Matériaux et Phénomènes Quantiques, Université Paris Cité - CNRS, Paris, France

*These authors contributed equally to this work

**Corresponding author:

a.koerner@fz-jueich.de, l.morales@fz-juelich.de, a.hutzler@fz-juelich.de

Applied terminology

The potential of any redox couple studied, including REs at equilibrium conditions, will depend on the reactions happening at the electrode-electrolyte interface. This potential can be

estimated using the Nernst equation (Eq.SI 1). Here, by considering the specific concentration of reactants used during the electrochemical experiments, and with the standard electrode potential E_0, the ideal gas constant R, temperature T, the Faraday constant F, the number of transferred electrons z_e, and the activity a of the oxidized (subscript Ox) and reduced species (subscript Red), respectively, the Nernst potential given in Eq. SI 1.[1–3]

$$E_{eq} = E_0 + \frac{RT}{z_e F} \cdot \ln\left(\frac{a_{Ox}}{a_{Red}}\right). \quad \text{(SI 1)}$$

In order to study electrochemical reaction kinetics with electron- and ion-transfer processes, the current transferred can be described *via* the Butler-Volmer equation (Eq. SI 2) with the current density j, which is the sum of the anodic (subscript a) and cathodic (subscript c) current contributions. Each current branch is defined by the exchange current density j_0, the charge transfer coefficient α, and the activation overpotential $\eta = E - E_{eq}$, with the electrode potential E and the equilibrium potential E_{eq}.[2,4]

$$j = j_a + j_c, \qquad j = 0\ \mathrm{A\ cm^{-2}}\ , \mathrm{equilibrium - OCP}$$

$$j = j_0 \cdot e^{\left(\frac{(1-\alpha)\cdot z_e \cdot F}{R \cdot T} \cdot \eta\right)} - j_0 \cdot e^{\left(\frac{-\alpha \cdot z_e \cdot F}{R \cdot T} \cdot \eta\right)} \quad \text{(SI 2)}$$

The equilibrium state at which the current flowing through the electrical circuit becomes net-zero, $j = 0\ A\ cm^{-2}$, is associated with a certain potential (open-circuit potential, OCP). For one redox couple, the system is described by the Nernst potential (Eq. SI 1). If more than one reaction is involved at the electrode-electrolyte interface, a mixed potential is established, which depends on the kinetics of all reactions involved. Nevertheless, also in this case, the sum of the anodic and cathodic currents is equivalent and cancels out.[5]

In situ experiments

The data analysis presented in the main manuscript is based on the following *in situ* experiments, and it is divided between Ag electrodeposition experiments and LSV experiments. The experiments were carried out once a stable response from the WE was achieved. This was aided, as in bulk electrochemistry, by performing an electrochemical cleaning of the WE.[6] Here, electrochemical protocols like CA, LSV, and OCP checks were employed. It is important to mention that the OCP evolution after the electrodeposition hold varies depending on the experiment, which could be explained by different relaxation paths depending on the dominant reactions at the electrode-electrolyte interface, or simply that certain experiments required more time than others to re-establish the equilibrium state. Still, similar trends can be observed between experiments *in situ*, as well as when compared to *ex situ* experiments.

Ag electrodeposition experiments:

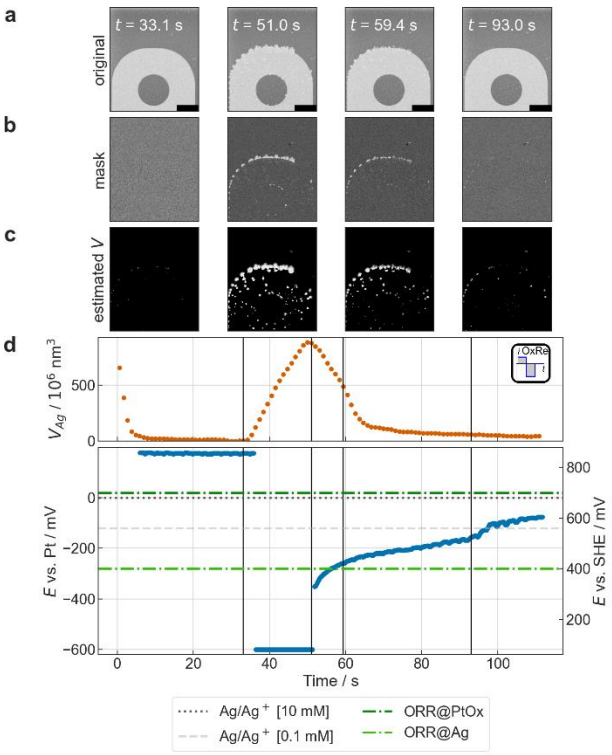

Figure SI 1: Analogous to Figure 2 for protocol Red, 1, video Experiment 1, Red.

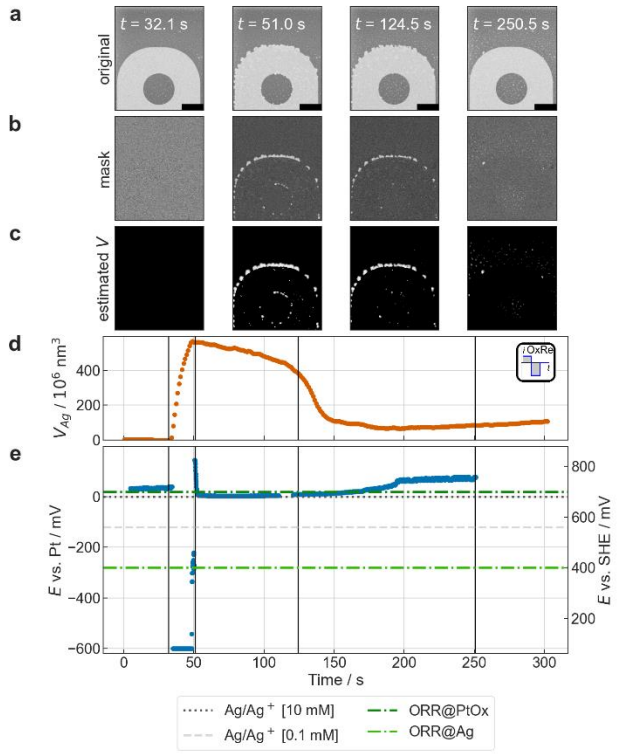

Figure SI 2: As shown in Figure 2 for protocol Red, 2, video Experiment 2, Red.

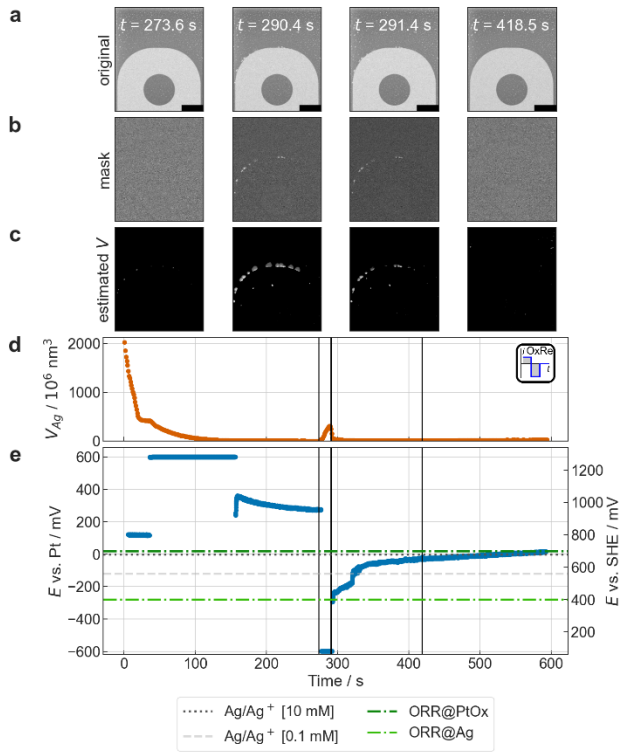

Figure SI 3: As shown in Figure 2 for protocol Ox-Red, 3, video Experiment 3, Ox-Red.

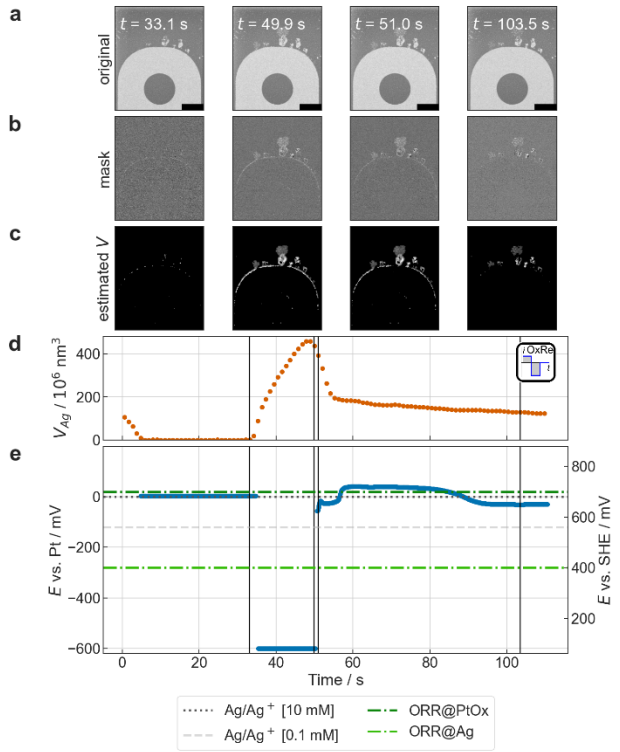

Figure SI 4: As shown in Figure 2 for protocol Red, 4, video Experiment 4, Red.

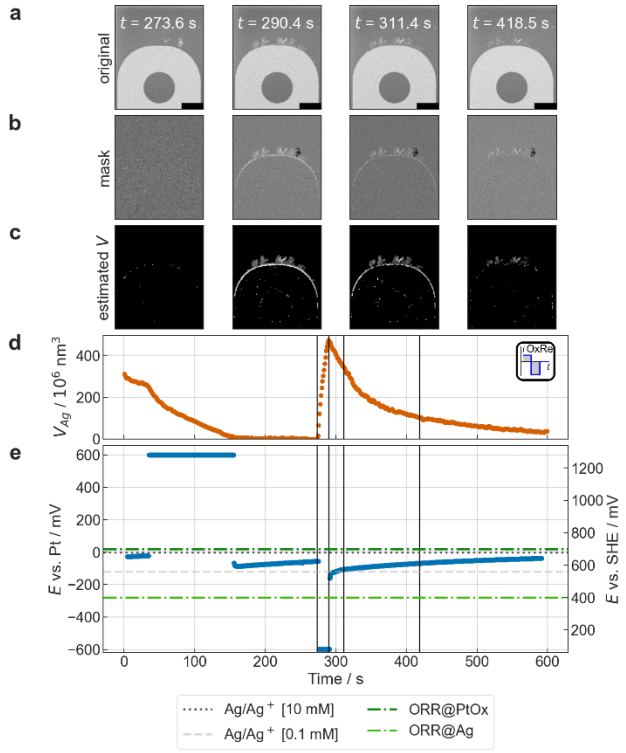

Figure SI 5: As shown in Figure 2 for protocol Ox-Red, 5, video Experiment 5, Ox-Red.

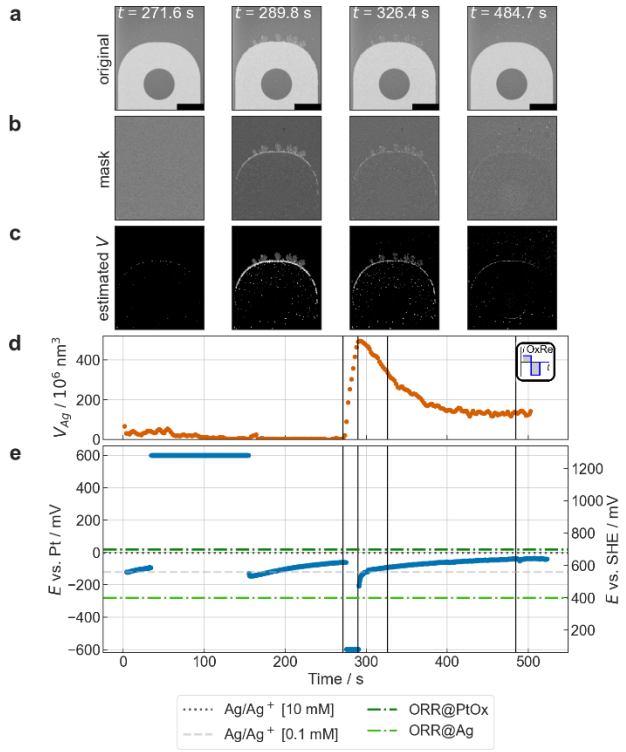

Figure SI 6: Figure 2 showing the complete protocol Ox-Red, 6, video Experiment 6, Ox-Red.

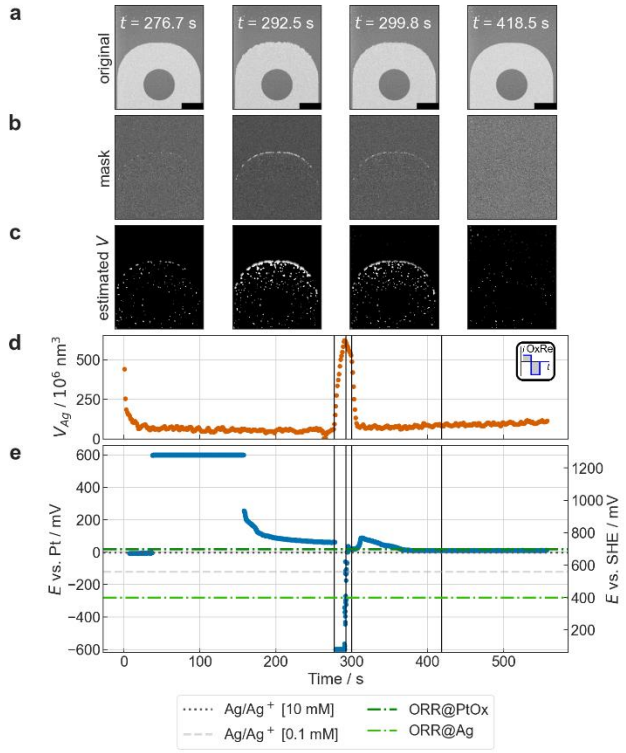

Figure SI 7: As shown in Figure 2 for protocol Ox-Red, 8, video Experiment 8, Ox-Red.

LSV experiments:

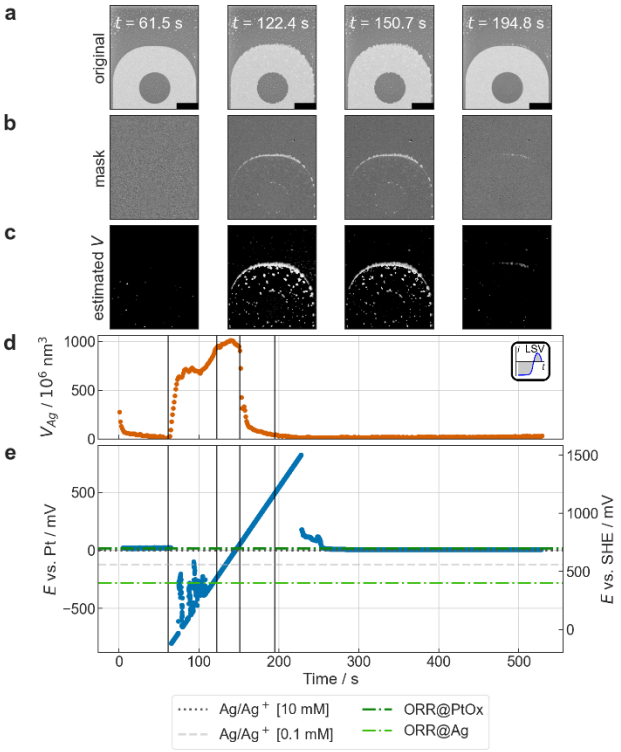

Figure SI 8: As shown in Figure 4 for protocol LSV, 1, video LSV 1.

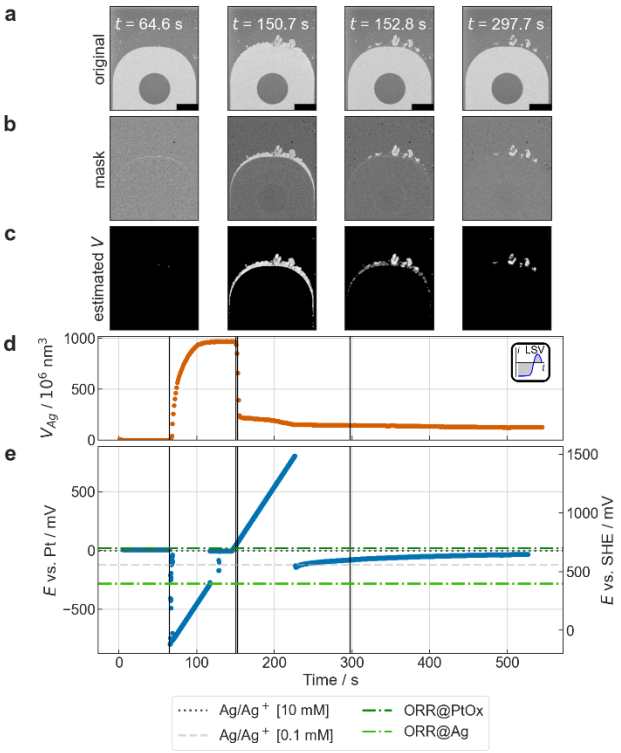

Figure SI 9: As shown in Figure 4 for protocol LSV, 2, video LSV 2.

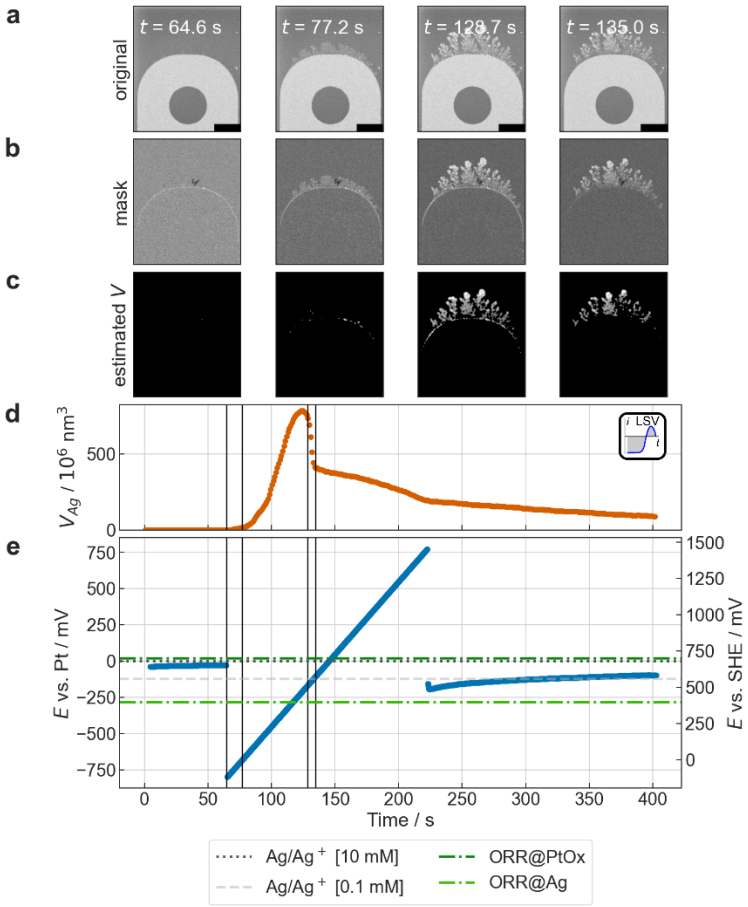

Figure SI 10: Figure 4, showing the complete protocol LSV, 3, video LSV 3.

The same experiments were conducted with a beam-off condition and followed the same protocol conditions as when the beam was on. Thus, in a similar way to IL-TEM, only the previous and after images were recorded.

Ag electrodeposition experiments carried out during beam-off conditions:

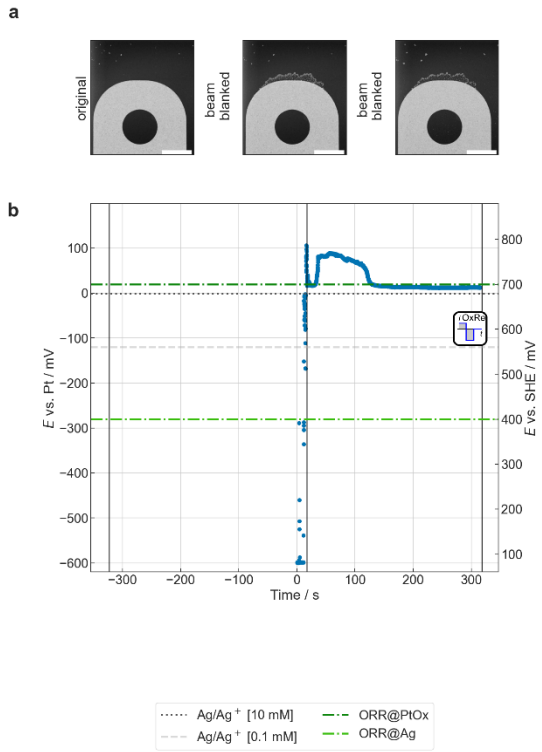

Figure SI 11: As shown in Figure 2 for protocol Ox-Red, 7, in situ IL-TEM. The sequence of images are: before the start of the protocol, start of OCP after Ag electrodeposition, end of OCP evolution after Ag electrodeposition.

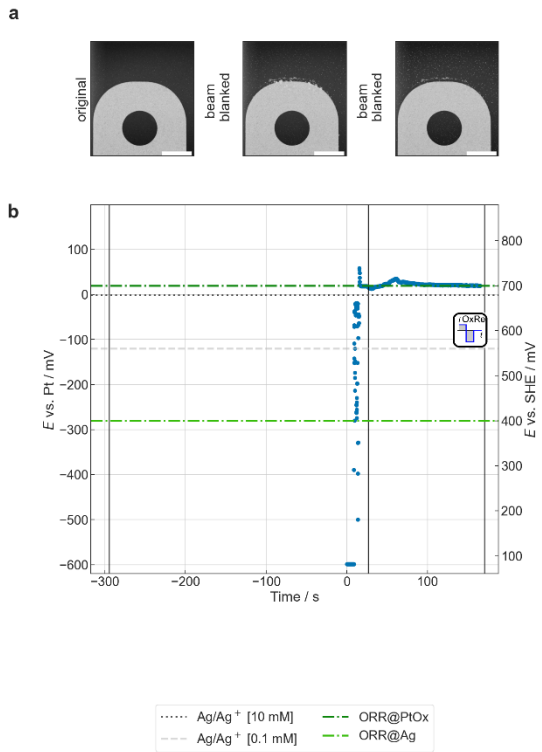

Figure SI 12: As shown in Figure 2 for protocol Ox-Red, 9, in situ IL-TEM. The sequence of images are: before the start of the protocol, start of OCP after Ag electrodeposition, end of OCP evolution after Ag electrodeposition.

LSV experiments experiments, beam off:

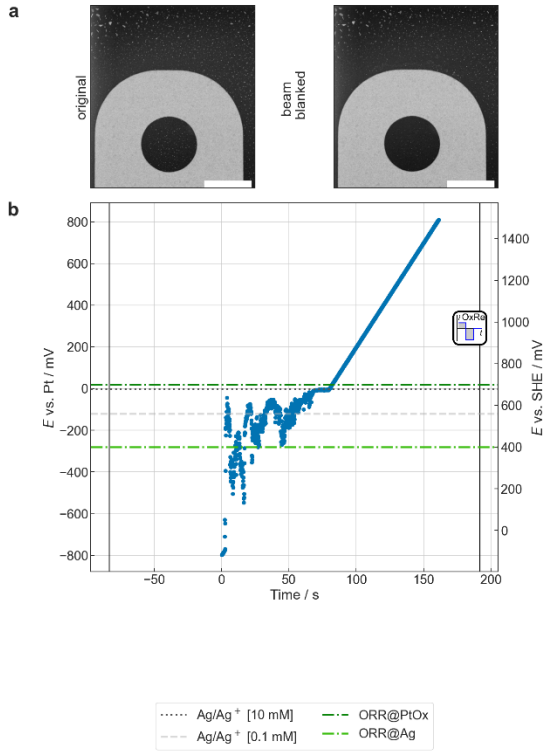

Figure SI 13: As shown in Figure 4 for protocol LSV, 4, in situ IL-TEM. The sequence of images are: before the start of the protocol, start of LSV ramp, and after the end of LSV ramp.

Theoretical electrochemical considerations

The construction of Pourbaix diagrams was aided by the Python package *Pourpy* developed by Korber, Furcas *et al*.[7] The thermodynamic data needed to calculate the stable phases were extracted, depending on their availability, from the following sources.[8,9]

Table SI 1: Reaction set used for constructing the Ag Pourbaix diagram.

	Reactions
1	$2H^{+1} + 2e^{-} \rightleftharpoons H_2$
2	$O_2 + 4H^{+1} + 4e^{-} \rightleftharpoons 2H_2O$
3	$Ag^{+1} + 1e^{-} \rightleftharpoons Ag$
4	$AgO^{-1} + 2H^{+1} + 1e^{-} \rightleftharpoons Ag\|0\| + H_2O$
5	$2AgO^{-1} + 2H^{+1} \rightleftharpoons Ag_2O + H_2O$
6	$Ag_2O + 2H^{+1} + 2e^{-} \rightleftharpoons 2Ag + H_2O$
7	$Ag_2O + 2H^{+1} \rightleftharpoons 2Ag^{+1} + H_2O$

8	$Ag_2O_2 + 2H^{+1} + 2e^- \rightleftharpoons Ag_2O + H_2O$
9	$Ag_2O_2 + 4H^{+1} + 2e^- \rightleftharpoons 2Ag^{+1} + 2H_2O$
10	$Ag_2O_2 + 2e^- \rightleftharpoons > 2\,AgO^{-1}$
11	$Ag_2O_3 + 2H^{+1} + 4e^- \rightleftharpoons Ag_2O_2 + H_2O$
12	$AgO^{+1} + 2H^{+1} + 1e^- \rightleftharpoons Ag^{+2} + H_2O$
13	$Ag_2O_3 + 2H^{+1} \rightleftharpoons 2AgO^{+1} + H_2O$
14	$Ag_2O_3 + 6H^{+1} + 4e^- \rightleftharpoons 2Ag^{+1} + 3H_2O$
15	$Ag_2O_3 + 2H^{+1} + 4e^- \rightleftharpoons 2AgO^{-1} + H_2O$
16	$Ag_2O_3 + 6H^{+1} + 2e^- \rightleftharpoons 2Ag^{+2} + 3H_2O$
17	$AgO^{+1} + 2e^- \rightleftharpoons AgO^{-1}$
18	$Ag(OH)_2^{-1} + 1e^- \rightleftharpoons Ag + 2\,(OH)^{-1}$
19	$Ag_2O_3 + H_2O + 2e^- \rightleftharpoons Ag_2O_2 + 2\,(OH)^{-1}$
20	$AgHO_2 + 1e^- \rightleftharpoons Ag^{+1} + (OH)_2^{-1}$
21	$2Ag^{+2} + H_2O \rightleftharpoons AgO^{+1} + Ag^{+1} + 2H^{+1}$

Table SI 2: Reaction set used for constructing the Pt Pourbaix diagram.

	Reactions
1	$2H^{+1} + 2e^- \rightleftharpoons H_2$
2	$O_2 + 4H^{+1} + 4e^- \rightleftharpoons 2H_2O$
3	$PtO + 2H^{+1} + 2e^- \rightleftharpoons Pt + H_2O$
4	$PtO_2 + 2H^{+1} + 2e^- \rightleftharpoons PtO + H_2O$
5	$'PtO_3 + 2H^{+1} + 2e^- \rightleftharpoons PtO_2 + H_2O$
6	$Pt^{+2} + 2e^- \rightleftharpoons Pt$
7	$PtO + 2H^{+1} \rightleftharpoons Pt^{+2} + H_2O$
8	$PtO_2 + 4H^{+1} + 2e^- \rightleftharpoons Pt^{+2} + 2H_2O$

Furthermore, the theoretical Nernst potential of the silver redox couple with a 10 mM Ag^+ concentration is calculated as follows:

$$E_{Ag/Ag^+} = E^{\circ}_{Ag/Ag^+} + \frac{RT}{nF} \cdot log([Ag^+]) \quad \text{(SI 3)}$$

This value will be calculated on the SHE scale, as the Ag redox couple is not pH dependent, as shown from reaction 3 in Table SI 1. Thus, the calculation continues as follows:

$$E_{Ag/Ag^+} = 0.799\ V_{SHE} + \frac{R\ (J\ mol^{-1}\ K^{-1}) \cdot T(K)}{n \cdot F(C\ mol^{-1})} \cdot log\left(\left[\frac{1}{0.01}\right]\right)$$

$$E_{Ag/Ag^+} = 0.68\ V_{SHE} \quad \text{(SI 4)}$$

This was confirmed experimentally, where a Ag WE was used to measure the OCP potential (Figure SI 14a). However, if a Pt WE is used, the OCP deviates slightly from the theoretical value (Figure SI 14b). Finally, the OCP value using a Pt electrode as RE *ex situ* with a Ag and Pt WE follows the same trend as *ex situ* (i.e., the OCP of Pt is slightly higher than the one using the Ag WE). Still, the OCP values obtained from the *in situ* data are replicated *ex situ* (Figure SI 14c, d), but with higher instability, as when measuring with a Ag/AgCl RE and then converted to SHE.

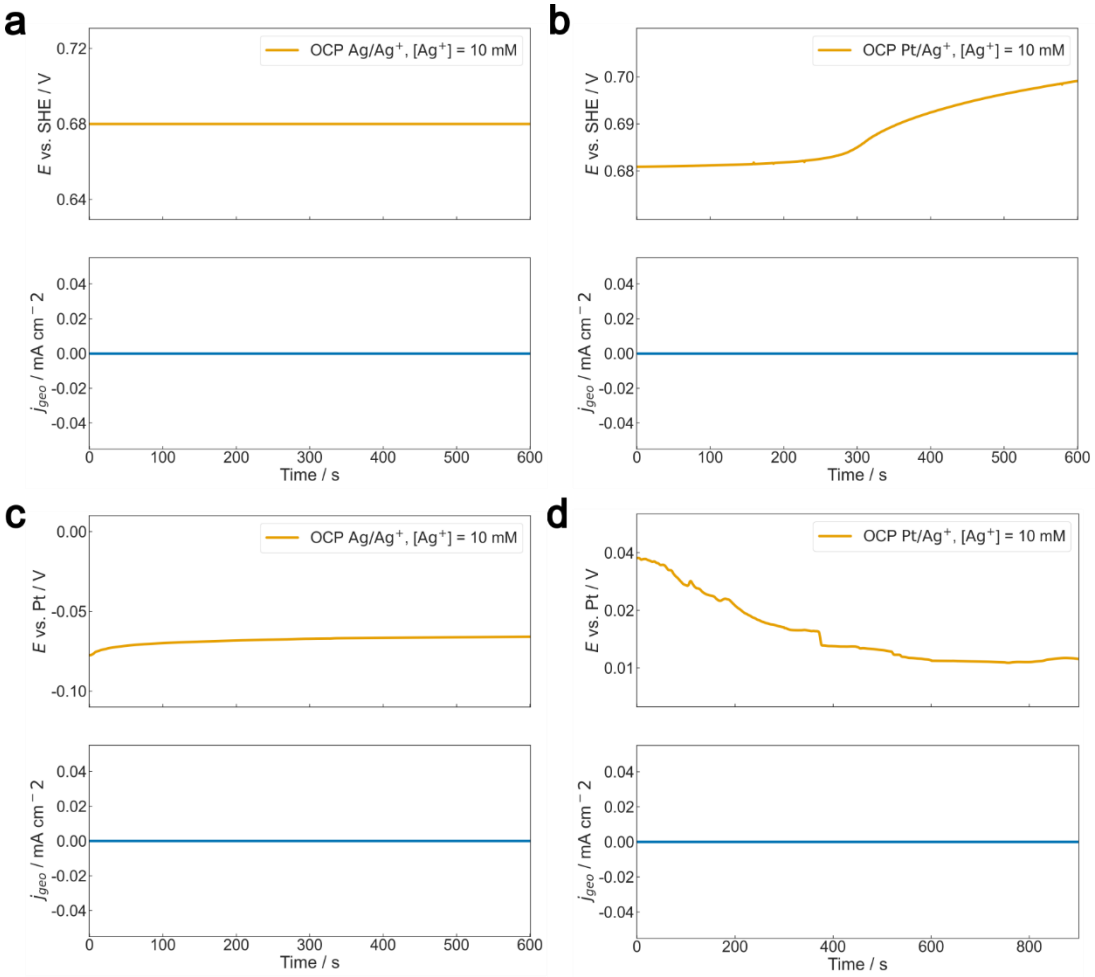

Figure SI 14: OCP values measured ex situ using a 10 mM $AgNO_3$ solution Ar-purged and a) a Ag WE, Pt CE, Ag/AgCl RE, b) a Pt WE, Pt CE, Ag/AgCl RE, c) a Ag WE, Pt CE, Pt pRE, and d) a Pt WE, Pt CE, Pt pRE.

To calculate the Nernst potential in the case where a possible depletion of Ag occurs just after stopping the electrodeposition hold, we also reduced the concentration from 10 mM to 0.1 mM. Assuming 0.1 mM of Ag^+ as the concentration, the theoretical potential calculated is 0.56 V vs. SHE.

This was simulated experimentally by using a 10 mM $NaNO_3$ solution instead of the $AgNO_3$ and measuring the OCP value obtained when using a Ag WE (Figure SI 15a).

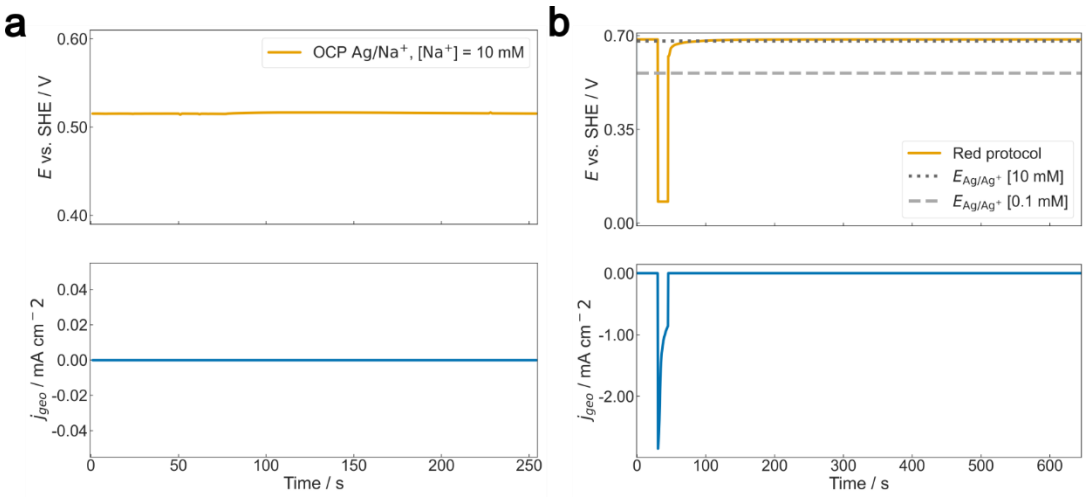

Figure SI 15: OCP comparison ex situ to simulate Ag^+ depletion scenario using a) a 10 mM $NaNO_3$ solution Ar-purged and b) a 10 mM $AgNO_3$ solution Ar-purged. Here, the protocol of electrodeposition of Ag on a Pt foil is shown (further details in section Quantifying silver dissolution with other setups). There, once the reductive hold is stopped, the potential at the start of the OCP is lower than the OCP expected of a 10 mM $AgNO_3$ solution, and after given time comes back to its expected value.

Although the experimental potential is lower than the theoretically calculated for a 0.1 mM $AgNO_3$, we show that the OCP of Ag when in contact with a 10 mM XNO_3 solution in the absence of Ag^+ is lower. This helps us understand the OCP evolution starting at lower potentials and then reaching the expected OCP (Figure 2, Figure SI 1-Figure SI 7), which we also observe *ex situ* during the electrodeposition experiment (Figure SI 15b). Thus, we can propose a local depletion of Ag^+ at the start of the OCP after electrodeposition. Still, we also acknowledge that possible artifacts arising from the potentiostat control could also cause this sudden start in OCP, but still, if given time, it evolves to the one expected in Eq. SI 4 and seen in Figure SI 15b.

Electrochemical data evaluation

The LSV protocols allow for the observation of electrodeposition and dissolution of Ag. At net zero current condition (anodic and cathodic reactions are balanced), the equilibrium potential is obtained as $LSV_{Equilibrium}$ from Tafel analysis, which is traditionally done by plotting the current logarithmically and extrapolating the linear (kinetically limited) regime of both reducing and oxidizing processes. The intersection point of these linear extrapolations

indicates the overpotential, the potential close to equilibrium, at which both processes happen at the same rate. The result is a net equilibrium where the anodic current equals the cathodic current, leaving the system with a zero current response across the external (measured) circuit. From this analysis, parameters like the exchange current density j_0 and the tafel slope, b, can be extracted as well. With the current j, the activation overpotential η can then be expressed as:

$$\eta = j_0 + b \log_{10}(j) \qquad \text{(SI 5)}$$

With our data, we decided to apply a Lorentzian fitting to estimate the peak position, which represents this net equilibrium. On each branch, before and after the peak, a region between 50 mV and 120 mV away from the fitted peak position was considered for the linear fit (assuming the mass transport limitation regime). The fitted function is shown as a line, and its extrapolation as a dashed line. The crosspoint of the extension of these determines the equilibrium voltage and the exchange current density.

The same protocols were repeated *ex situ* but using a Ag/AgCl RE with saturated KCl, which allows the conversion of the $\mathrm{LSV_{Equilibrium}}$ obtained *ex situ* to the SHE potential scale *via* Eq. SI 6.

$$E_{\text{vs. SHE, } ex\,situ} = \mathrm{E_{Ag/AgCl}} + 0.2\ \mathrm{V} \qquad \text{(SI 6)}$$

This potential was then compared to the equilibrium potential obtained *in situ* using the Pt scale. The shift between these two potentials was then used to convert all the values obtained *in situ* vs. Pt to the SHE scale as follows:

$$\Delta E_{\text{Equilibrium vs. SHE, } in\,situ} = \mathrm{E_{Equilibrium\ vs.\ SHE,}\ ex\,situ} - \mathrm{E_{Equilibrium\ vs.\ Pt,}\ in\,situ} \qquad \text{(SI 7)}$$

This shift is then added to the potentials vs. Pt to convert the *in situ* potentials to the SHE as follows in Eq.SI 8. No ohmic correction was done *in situ* or *ex situ*.

$$E_{\text{vs. SHE, } in\ situ} = E_{\text{vs. Pt, } in\ situ} + \Delta E_{\text{Equilibrium vs. SHE, } in\ situ} \quad \text{(SI 8)}$$

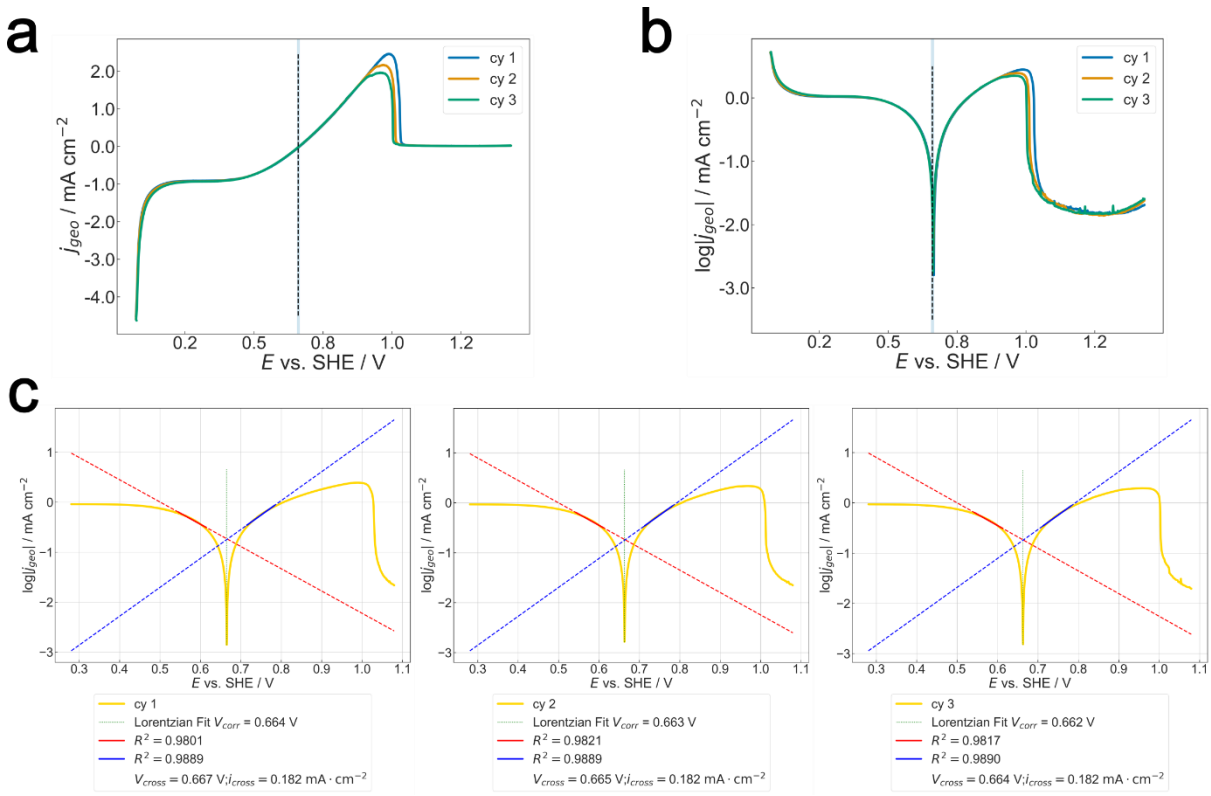

Figure SI 16: LSV cycles for potential equilibrium determination ex situ: a) and b) show the obtained data from LSVs in current density and semi-log current density versus potential. c) exemplary data analysis of the cycles presented previously.

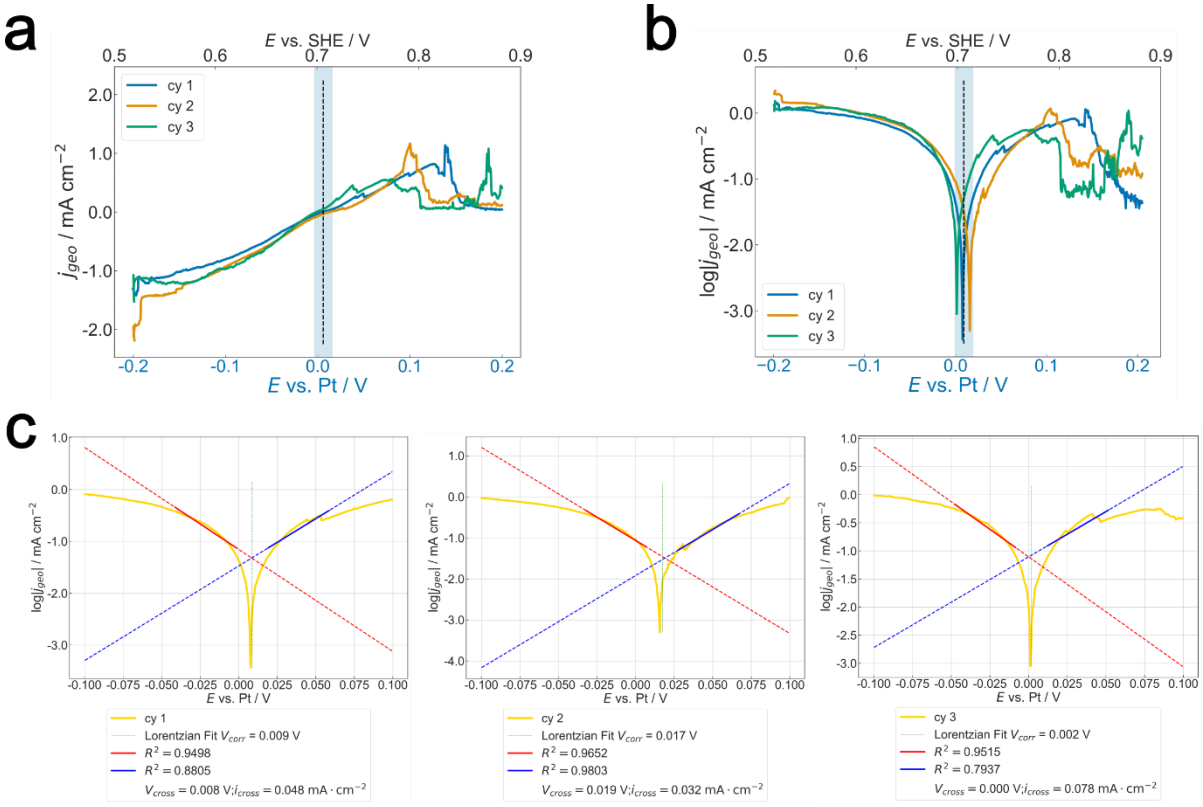

Figure SI 17: LSV cycles for potential equilibrium determination in situ: a) and b) show the obtained data from LSVs in current density and semi-log current density versus potential. c) exemplary data analysis of the cycles presented previously.

Material quantification using charge integration

To compare the material deposited from the volume analysis and the current response, we integrated the current to obtain the charge during the electrodeposition holds or stripping steps. The charge was converted to mass using the Faraday constant and the molar mass of the Ag, and assuming that all the current is used to deposit Ag, *ex situ* and *in situ.* From there, the FE efficiency of the process was quantified. From this we see that after several cycles and extending the window potential of the ramp during LSVs, the FE tends to decrease. *In situ*, a clear advantage of a ramp with a smaller window potential is observed, since the potential is much better controlled.

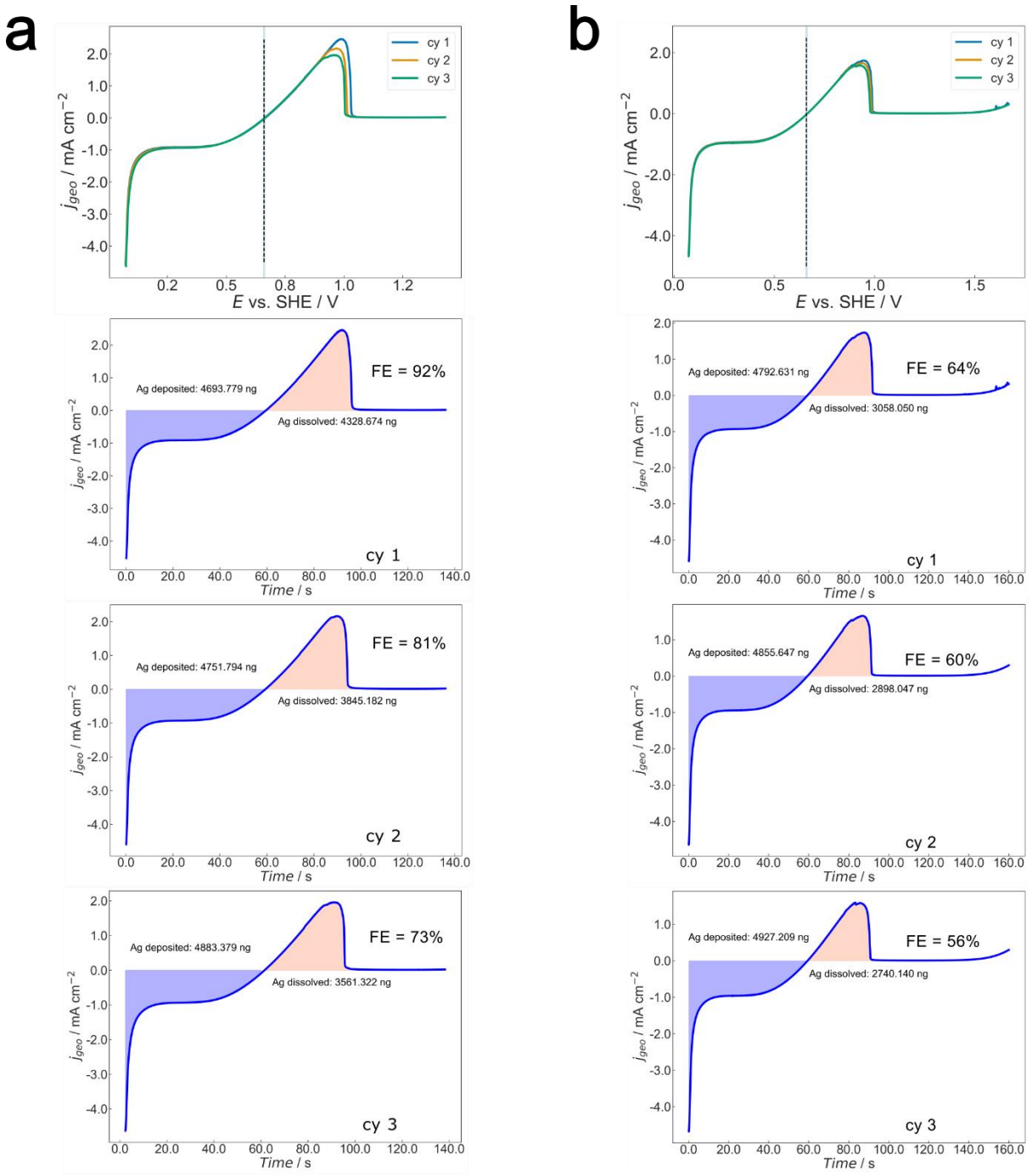

Figure SI 18: LSV for FE quantification ex situ: a) Lower UPLs show to achieve higher FE along the cycling. b) higher UPLs show a decrease in FE along cycling.

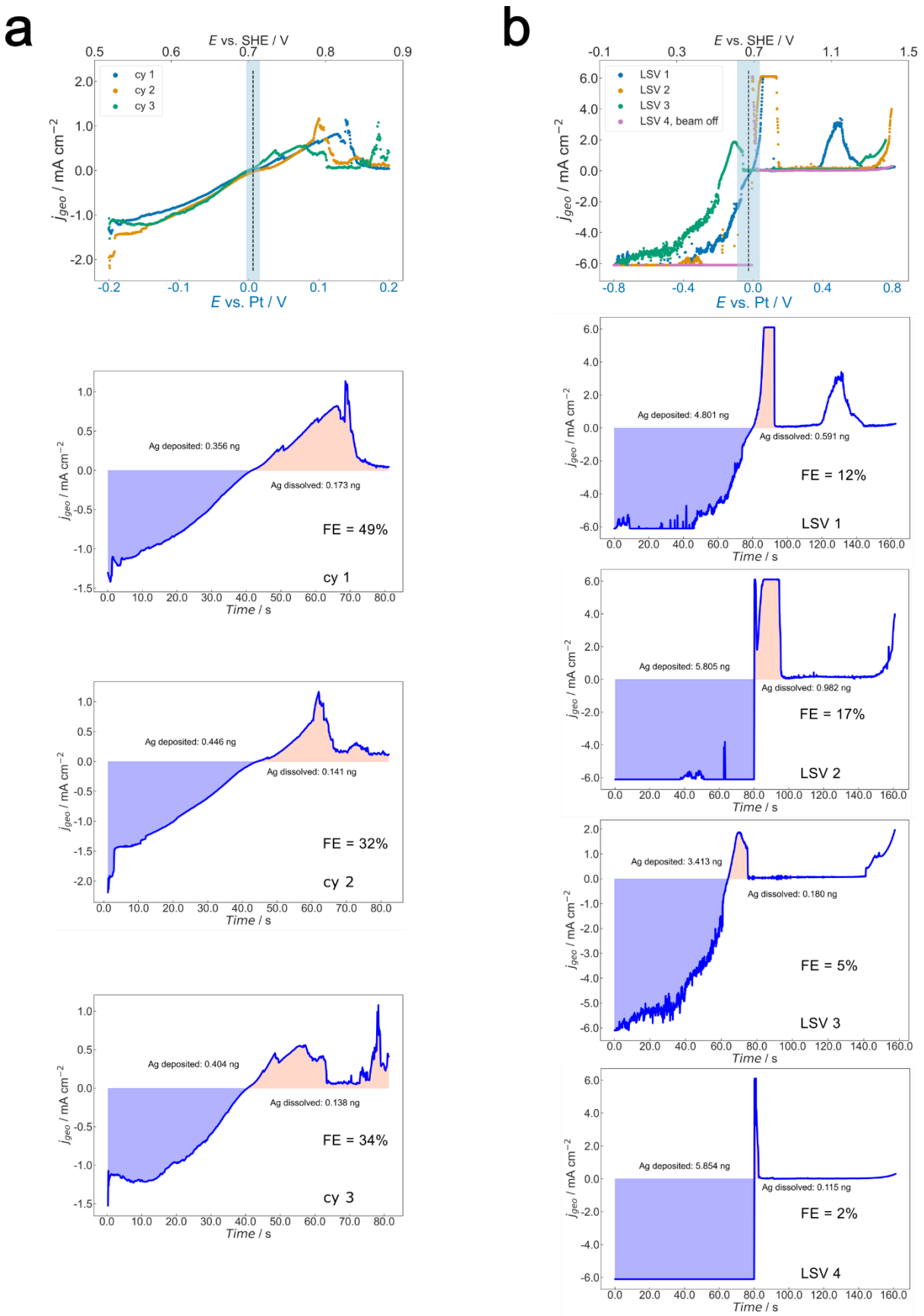

Figure SI 19: LSV for FE quantification in situ: a) Lower UPLs show that higher FE can be achieved along the cycling, but still lower value compared to the ex situ experiments. The image series of these LSV are shown in video, LSVcy1-3, and LSV1-LSV3. Due to the higher contrast inversion attributed to a higher amount of Ag

electrodeposited, the volume calculation is not accurate. Therefore, they are not displayed and considered in Table 2 for YRV% vs FE% comparison in situ. b) Higher UPLs show a detrimental decrease in FE along cycling. Under this condition, the potential goes into momentary overloads. The images of these experiments are shown in Figure 5, Figure SI 7, and Figure SI 10.

Similar to the calculation for LSV cycles, the electrodeposited material in each experiment was calculated in a similar manner. These calculations assume that all the current drawn is used for the electrodeposition of Ag, which, as we have discussed, is not completely accurate since other competing reactions influence this reductive current response.

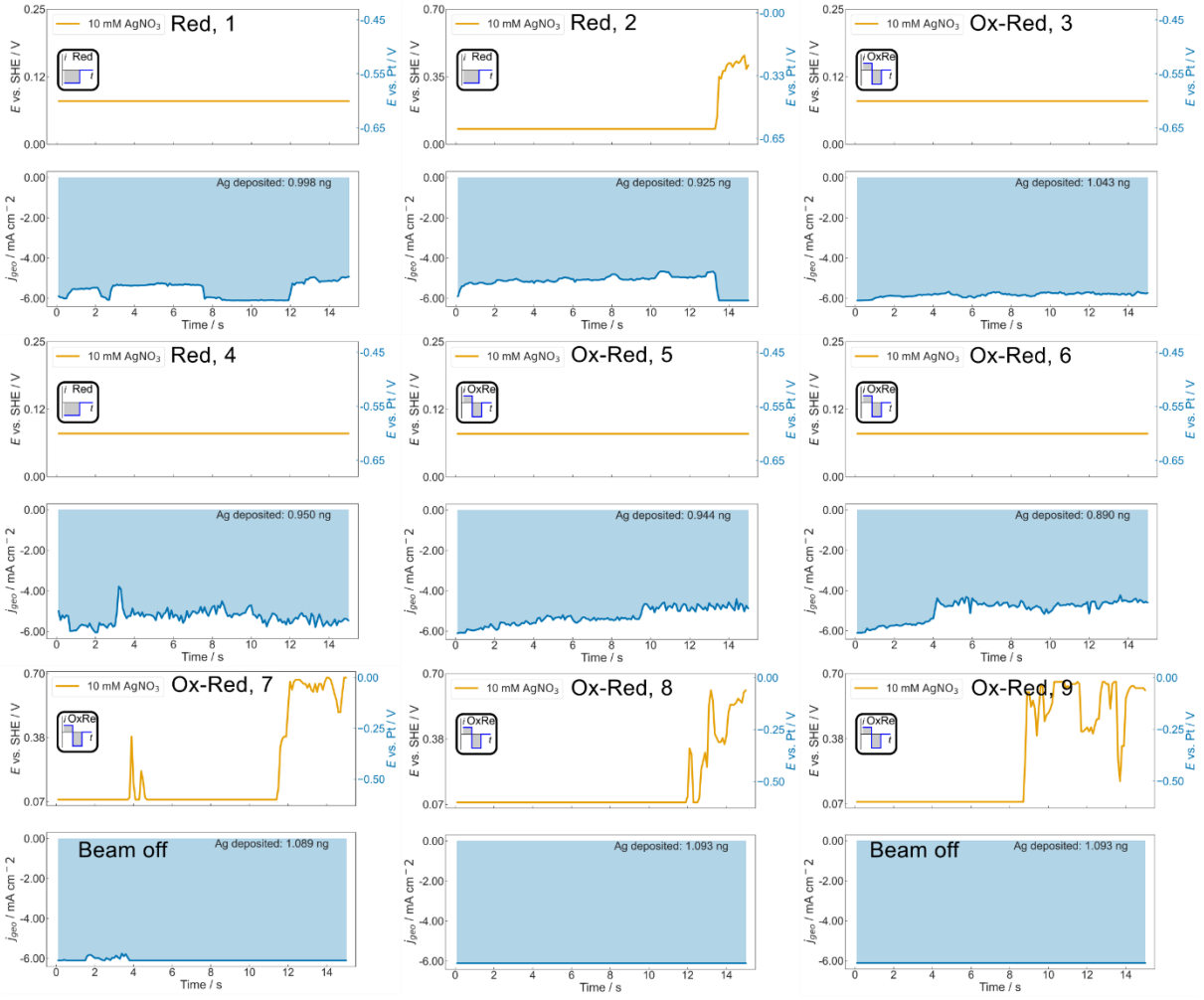

Figure SI 20: Material quantification from the electrodeposition holds in situ. The experiments are ordered chronologically. From here, we can also mention the deterioration of potential control, especially observed in the last experiments, where potential jumps are more pronounced and longer. The images of these experiments are shown in Figure SI 1.-Figure SI 7, and Figure SI 11-Figure SI 12.

Availability of oxygen for ORR_{Pt}

The dissolved volume of silver $V_{Ag,1}$ within the time t_1 (which corresponds to the quick dissolution event) is assessed at different flow rates. With the molar density of silver of ca. 0.0973 mol/cm^3, the number of silver atoms dissolved per second is as follows in Eq.SI 9, which is equivalent (see Eq. 2) to the number of electrons that are required to be transferred in the redox reaction.

$$\Delta n_{Ag,1} = \frac{V_{Ag,1}}{t_1} \cdot 0.0973 \ \frac{\text{mol}}{\text{cm}^3} \qquad \text{(SI 9)}$$

This quantity for each experimentally obtained amount of silver is indicated as red circles in Figure SI 22 in agreement with the respective flow rate read at each experiment. As every oxygen molecule requires 4 electrons (see Eq. 1), $\frac{\Delta n_{Ag,1}}{4}$ of O_2 is needed to consume these electrons.

Mass transport of O_2 to the electrode occurs *via* convection and diffusion. Flow of the solution is measured volumetrically (f) and with the geometry of the nanochannel (width $w = 500$ µm, height assumed to be the spacer thickness $h = 200$ nm) can be calculated into a flow velocity $v = \frac{f}{w \cdot h}$. A volume element of solution stays in contact with the working electrode while flowing over its length, approximated at $l = 200$ µm, for a time $t_s = \frac{l}{v}$ and is replaced at a turnoverrate of $t'_o = \frac{v}{l} = \frac{1}{t_s}$. During that contact time, the ions in the solution can diffuse in three dimensions by a length[10] $\Delta x = \sqrt{6Dt}$. The diffusion perpendicular $\Delta x_\perp$ to the chip-plane can be limited by the height of cell ("above the electrode"), so, if $\Delta x > h$, then $\Delta x_\perp = h$, else $\Delta x_\perp = \Delta x$. Diffusion parallel to the plane $\Delta x_\parallel$ is limited by the width of the nanochannel, assuming the working electrode is placed in the center, so, if $\Delta x > \frac{w}{2}$, then $\Delta x_\parallel = \frac{w}{2}$, else $\Delta x_\parallel = \Delta x$. The geometry of this estimation is highlighted in Figure SI 21.

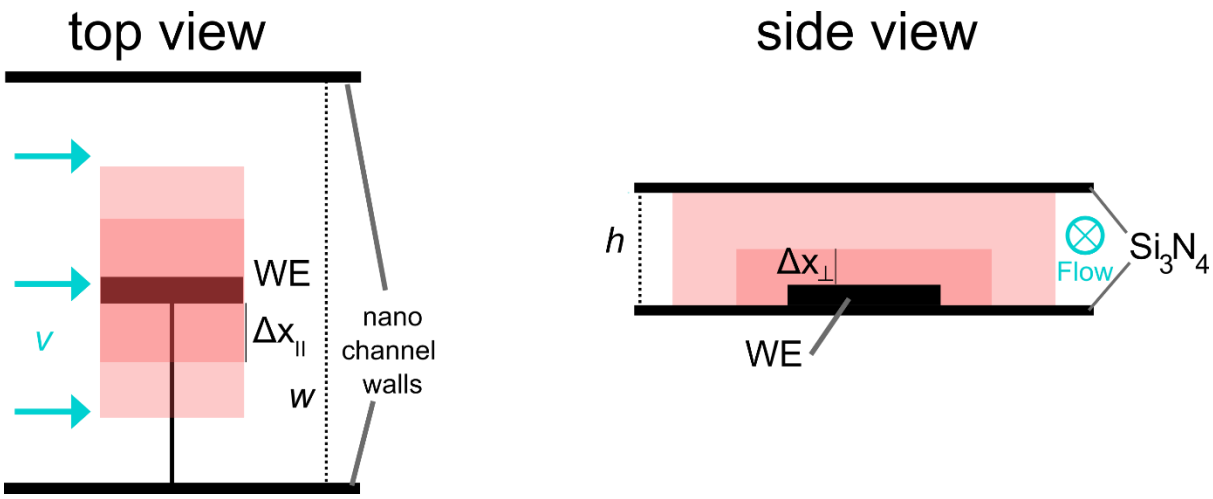

Figure SI 21: Geometry and parameters used to estimate the O2 available from diffusion.

The cuboid above the WE with volume $V_z = \Delta x_\perp \cdot A_{WE}$, and the cuboids adjacent to the WE, each with the volume $V_y = \Delta x_\parallel \cdot \Delta x_\perp l$, then contribute to the total volume of the solution element $V_{VE} = V_z + 2 \cdot V_y$ which allows O_2 to diffuse to the electrode surface. With the turnover rate t'_o an effective volume flow per second can be calculated as $V'_{eff} = t'_o \cdot V_{VE}$. The amount of available oxygen Δn_{O_2} then is related to the concentration of O_2 in the solution c_{O_2} as $\Delta n_{O_2} = V'_{eff} \cdot c_{O_2}$, with V'_{eff} being dependent on the volumetric flow rate f. C_{O_2} is unknown, as DI-water is used in the experiments, but atmospheric oxygen will diffuse into solution while the experiment is set up. However, the saturation concentration under standard conditions, often assumed at around $0.255\ \frac{\text{mmol}}{\text{L}}$, sets an upper limit.[11] By setting $\Delta n_{e^-}^{ORR}$ (blue curve, Figure SI 22), consequently above the experimentally obtained Δn_{Ag}, we can estimate which fraction of saturation concentration is needed. The rather low value of ~3.1% of the saturation concentration of O_2 indicates that more than enough O_2 would be available to accept electrons to drive the dissolution of Ag. ORR-driven dissolution of Ag, therefore, is plausible.

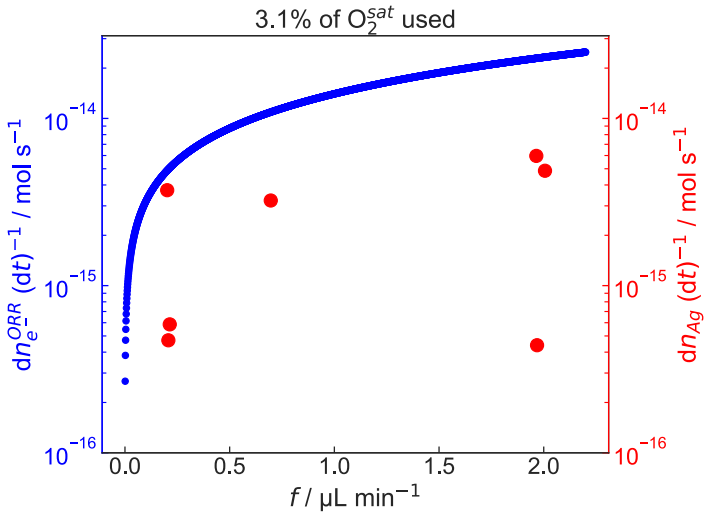

Figure SI 22: Demand of electrons from ORR (blue) is comparable to the number of electrons available from silver dissolution (red) each second.

Only a small fraction of this oxygen will typically contribute to the ORR under these experimental conditions. Several factors might limit the effective utilization of O_2: (i) from oxygen molecules within the diffusion-accessible volume, only those near the electrode have a chance to directly participate in the reaction. To drive diffusion efficiently, significant concentration gradients must be established first. (ii) Not all oxygen that reaches the electrode encounters an available reaction site immediately, leading to kinetic limitations. Last, (iii) the actual dissolved oxygen concentration may be substantially below the saturation value, depending on the duration and efficiency of gas exchange between air and the solution prior to the experiment, a quantity that is difficult to quantify precisely. Still, ORR *ex situ* experiments using a Pt electrode and a 10 mM $NaNO_3$ solution, with pH adjusted to 5, showed from the charge integration calculation that only a concentration of ~34.2 ± 7.4 µM of O_2 is reduced at these experimental conditions, even when having a solution constantly purged with oxygen (further details below in chapter Charge quantification for ORR *ex situ*).

Availability of oxygen for ORR_{Ag}

When silver particles become disconnected from the working electrode, they continue dissolving at a much slower pace (usually one order of magnitude slower). Like the estimation done above, the amount of oxygen that would be required to drive this dissolution is estimated analogously. The model particle which oxygen diffuses to is a square with 40 nm (~2x2 pixel^2) side length ($l = w = 40$ nm, $A = 1.6 \cdot 10^{-15}$ m^2).

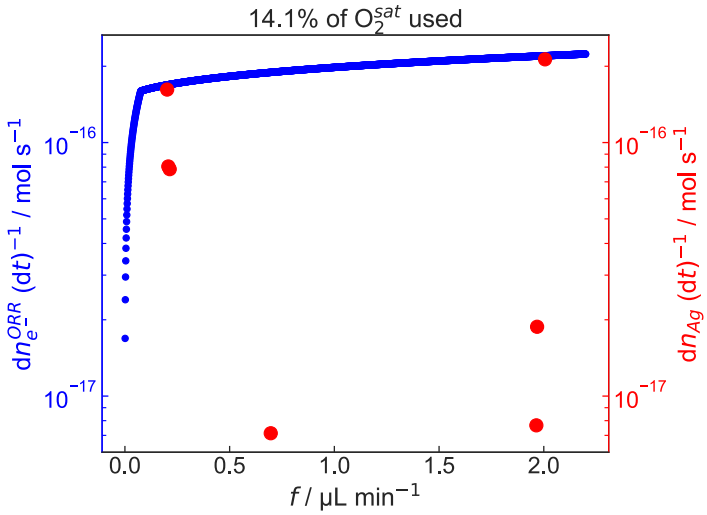

Figure SI 23: Analogous to Figure SI 22, but considering Ag as the electrocatalyst.

Based on this estimation, effectively only ~14% of the saturation concentration of oxygen is utilized to cause silver dissolution. The apparent discontinuity in the blue curve is explained by the dependence of the effective volume on the volumetric flow rate f for the volume adjacent (perpendicular to the flow direction in the plane of the chip) to the particle. Here, the effective volume depends on the diffusion length in two dimensions: in the height (perpendicular to the chip plane) and the direction perpendicular to the flow in the plane of the chip. Both diffusion lengths are proportional to $f^{-\frac{1}{2}}$. When calculating the effective volume, the multiplication of both lengths and the turnover rate (which is proportional to f^1), the effects cancel out and the diffusional available volume adjacent to the particle becomes independent of the flow velocity (unless it is restricted by the boundaries of the channel,

which is the case for slow flow). For the diffusion from above the particle, the diffusion length (also proportional to $f^{-\frac{1}{2}}$) is multiplied by the area of the particle and the turnover rate, to yield a dependence of $f^{\frac{1}{2}}$. Therefore, the effective available volume continues to grow with faster flow velocities.

During the reductive hold to deposit silver, parasitic reactions may draw a significant amount of current. And ORR is a likely candidate, as oxygen is present in the system, and the reductive potential accelerates the catalyzed ORR_{Pt}. Assuming the oxygen concentration estimated above as an upper boundary limit, we can estimate a maximum of current that could be drawn to ORR. The current can be calculated with the Faraday constant F *via* $I^{ORR} = \frac{\mathrm{d}n_{e^-}^{ORR}}{\mathrm{d}t} \cdot F$.

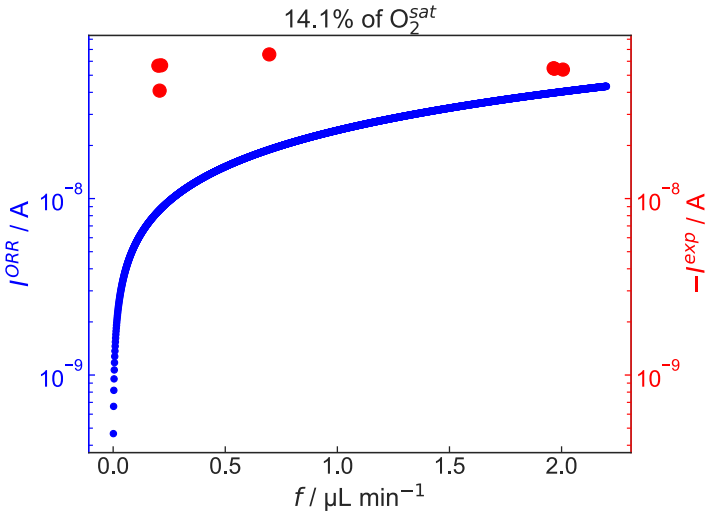

Figure SI 24: A significant amount of current during reductive growth might be drawn to ORR (blue datapoints). The concentration of oxygen assumed is $3.4 \cdot 10^{-5}\ mol\ L^{-1}$ *as calculated from ex situ ORR experiments (discussed below) and compared to our in situ experimental values.*

Especially at high flow rates, the current that could potentially go into ORR becomes significant, but also at lower flow rates could make up more than 10% of the deposition current. This parasitic current may contribute to the low YRV of *in situ* experiments presented in Table 1, 2.

Charge quantification for ORR *ex situ*

To have an estimation of how much of the current can be attributed to ORR from the electrodeposition experiments, we performed experiments *ex situ* where we replicated the experimental conditions during the reductive holds (pH and deposition potential). The difference is that a 10 mM $NaNO_3$ solution exposed to air and saturated with O_2 was used. From there, comparing the currents obtained from electrodeposition experiments (~6 mA) and the ORR experiments (~0.3 mA), we can estimate that at least 5% of the current is not used for Ag electrodeposition. Furthermore, the amount of O_2 possible to be converted into H_2O, assuming a $4e^-$ reaction process, calculated from this current, was by far below the limit of O_2 saturation when dissolved in the electrolyte. This could be attributed to the sluggish ORR, which is kinetically hindered. This is further sustained when comparing the electrolyte exposed to air or O_2-saturated conditions, where the results do not differ significantly.

It is important to mention that the *ex situ* cell has a finite reservoir of O_2, which implies that ORR becomes diffusion-limited, which then promotes the reduction of silver ions to elemental silver. This mechanism is not active in the LP-EM setup, as fresh electrolyte (and therefore oxygen) is continuously replenished. The ORR current responses *ex situ* do not vary drastically when using an O_2-purged $NaNO_3$ solution, showing once more that ORR is rather diffusion-limited.

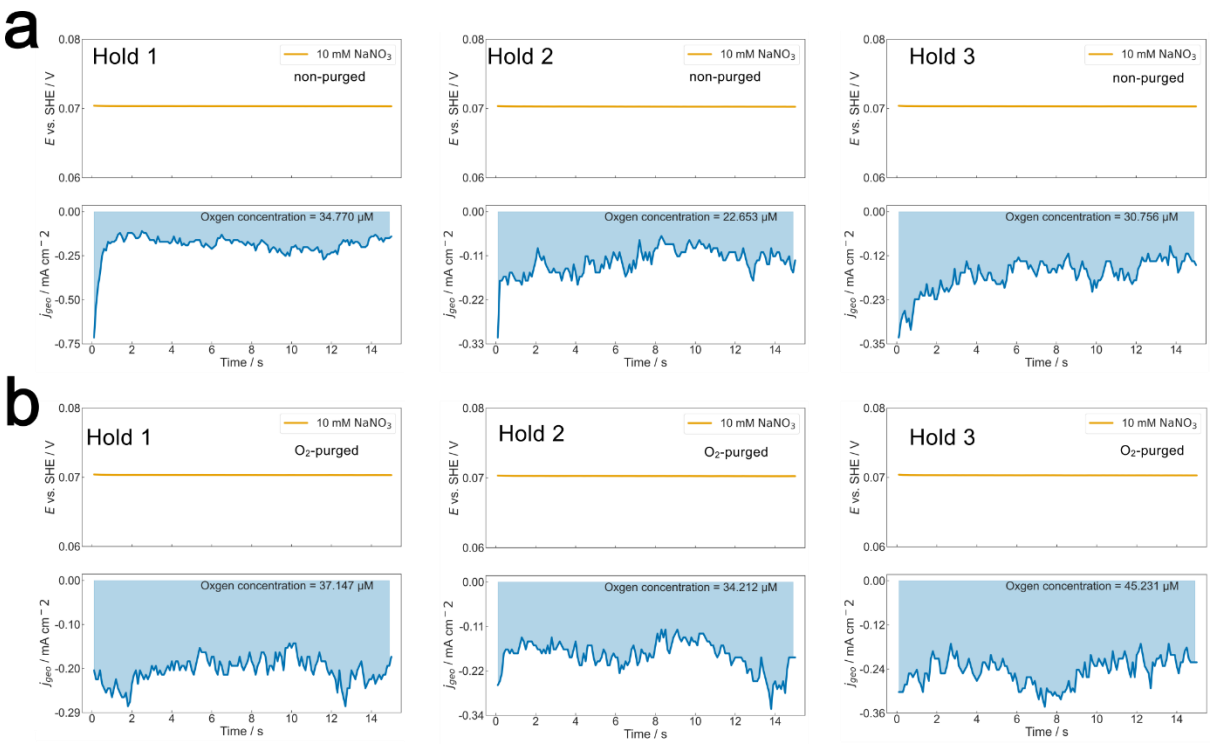

Figure SI 25: Ex situ estimation of ORR contribution during Ag electrodeposition holds. Three continuous electrodeposition holds are shown to see the comparison when oxygen is supplied or not: a) using a 10 mM $NaNO_3$ solution, non-purged but exposed to air. b) using the same solution, saturating it with O_2.

Quantifying silver dissolution with other setups

Silver was electrochemically deposited from 10 mM $AgNO_3$ solution onto platinum foils as shown in Figure SI 26.

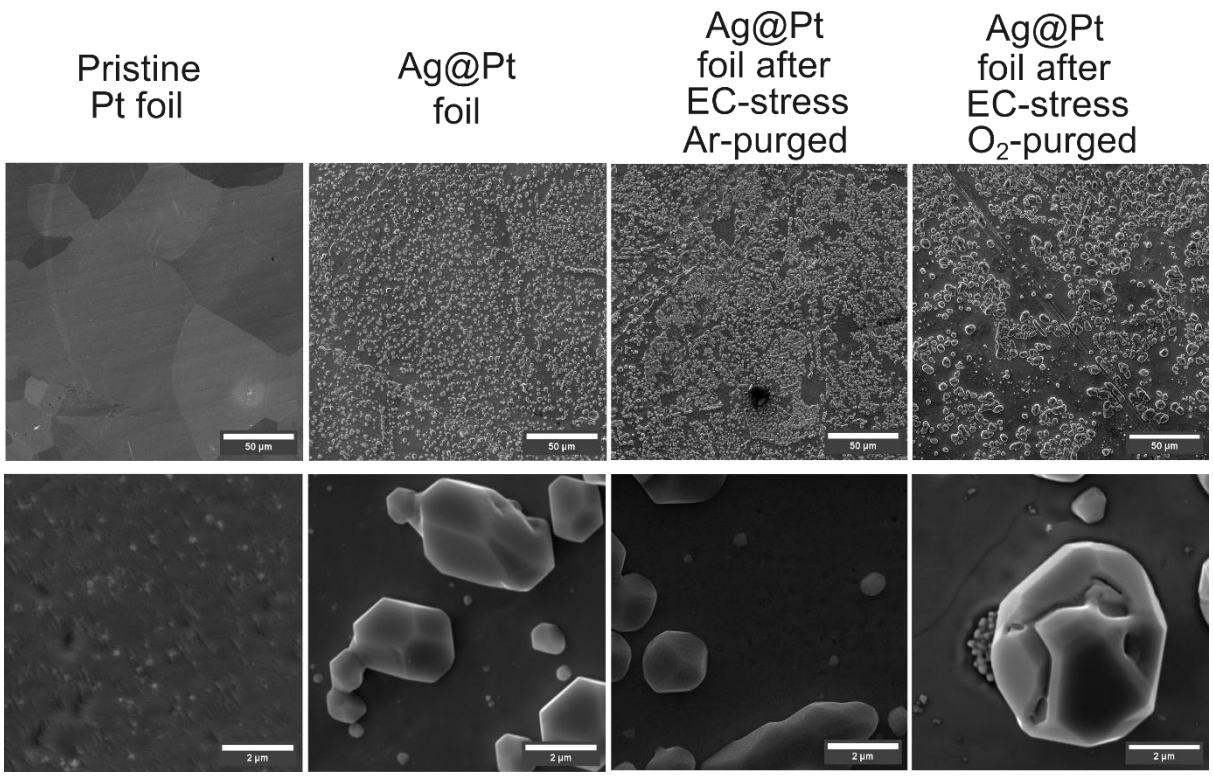

Figure SI 26: SEM images of Pt foils for SFC-ICP-MS experiments.

These Ag on Pt foils were then used as substrates for ICP-MS measurements. Silver showed dissolution while a zero current through the external circuit was enforced, and the corresponding potential was monitored *via* OCP measurements (Figure SI 27). This supports our claim that silver is dissolved sacrificially. Platinum, however, does not dissolve in significant amounts.

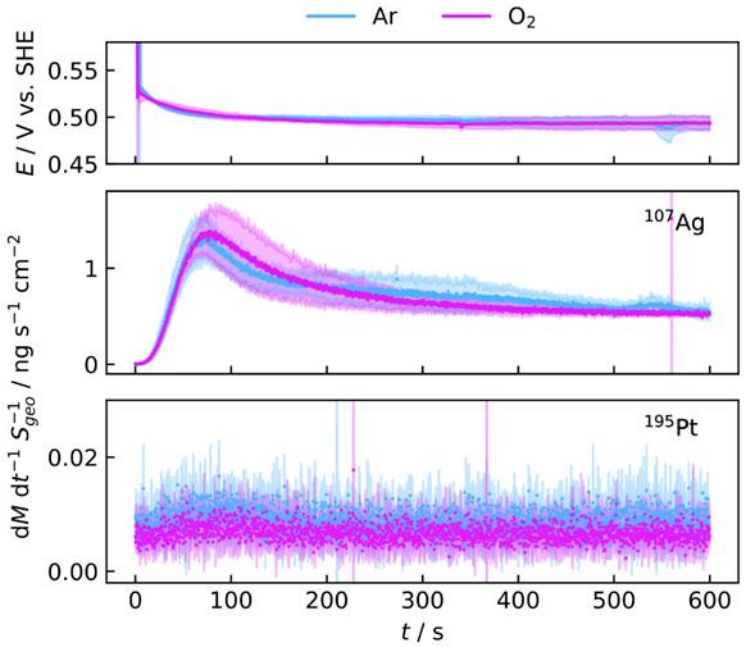

Figure SI 27: SFC ICP MS measurement of Ag@Pt in $NaNO_3$. From top to bottom: Measured open-circuit potential and Ag dissolution rates on three independent sample locations (dark to light), purging with Argon and Oxygen. No detectable difference of Ag dissolution between both gases. Pt dissolution not detected.

Influence of the scattering from the electrode

Inelastic scattering of primary electrons deposits energy into the material, introducing beam damage or radiolysis. As the inelastic mean free path heavily depends on the atomic number, heavier atoms will scatter electrons much more, depositing more energy into the system. Water, as the main component of the electrolyte, only contains light elements and therefore has a low interaction probability, whereas the Pt electrode has a much higher inelastic scattering probability. SE emitted because of inelastic scattering, in turn, have a high probability of interaction due to their low energy, and could significantly enhance the effective dose rate within the electrolyte in proximity to the electrode. As this can alter the radiolytically triggered processes, such as growth and dissolution, the impact of secondary electron emission is evaluated here.

We approach the issue with Monte-Carlo simulations of electron trajectories performed in CASINO [12] in a simplified cell geometry. The average energy change due to electron-water interactions can then be related to the dose rate.

The cell constructed in CASINO represents a 1 µm x 1 µm area of the cell and consists of two 30 nm thick slabs of silicon nitride (Si_3N_4) representing the viewing windows. Between is a 200 nm thick slab with electrolyte, approximated as homogeneously distributed water H_2O with 55.56 mol L^{-1}, and 10 mmol L^{-1} of $AgNO_3$. In total the ratio of the elements therefore becomes 11111 (H): 5558 (O): 1 (N): 1 (Ag). The Si_3N_4 - H_2O + $AgNO_3$ - Si_3N_4 layered structure represents the left half (negative x) of the cell. In the right half (positive x) of the simulated volume, the water/electrolyte slab is only 130 nm thick. The remaining 70 nm are replaced with platinum, representing the electrode. The model is depicted in Figure SI 28.

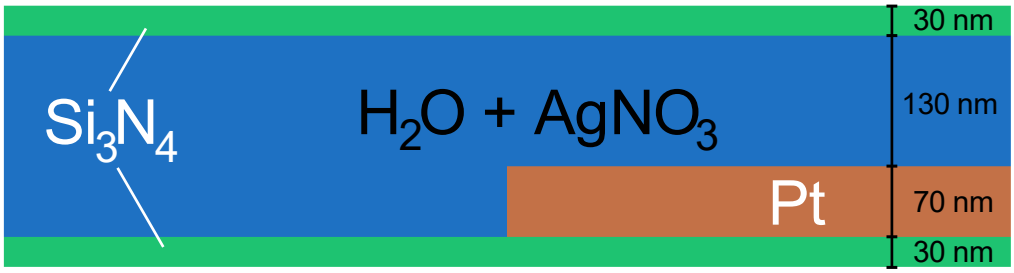

Figure SI 28: Side view of the simplified geometry of the cell as simulated in CASINO. Each component extends 1 µm into the plane of the figure.

We simulated 1000 electrons, each in 201 scan points ranging from x = -100 nm to + 100 nm, with 0 nm being the edge of the Pt-electrode. The default set of model and parameters for MONSEL is described by Lowney[13] with a Lagged Fibonacci (Boost If607) as a random number generator, a directing cosine suggested as described by Lowney[13,14], and a minimum electron energy of 0.05 eV for the threshold of secondary generation was selected, as well as a maximum order of SE generation of 10. The residual energy loss was set to 0.0004 eV, and the acceleration voltage was set to 200 keV.

From the simulated trajectories, each event causing a negative energy change (i.e., from the primary electrons to the material) is considered as an inelastic scattering event. The energy changes were binned into x-coordinates with 1 nm step size and summed. This summed

energy is then divided by the volume the energy is distributed over to yield an energy density $\rho_E^V = \frac{\Delta E}{V}$. With the density of water ($\rho_{H_2O} = 997\,\frac{\mathrm{kg}}{\mathrm{m}^3}$) an energy mass density is calculated $\rho_E^m = \frac{\rho_E^V}{\rho_{H_2O}}$. By dividing by the number of incident electrons n_{e^-}, the dose rate per electron is given $\frac{\Psi}{n_{e^-}} = \frac{\rho_E^m}{n_{e^-}}$. The results are on the same order of magnitude (for pure 200 nm water, around factor of 2) compared to established dose rate calculations [15,16] *via*. Eq. SI 10

$$\Psi = \frac{\phi}{e} S \left(1 + \frac{z_l}{\lambda_{IMFP}}\right) \tag{SI 10}$$

With the inelastic mean free path $\lambda_{IMFP} = 380$ nm; the stopping power $S = 2.84$ MeV cm^2 g^{-1} (for 200 keV;[17] assuming 1 $e^-/1000\,nm^2$ in $z_l = 200$ nm of water)

In the simulated energy distribution for the simplified cell described above (see Figure SI 28), the dose rate does not increase significantly near the solid-liquid interface (at $x = 0$ nm). In the region of the platinum electrode ($x > 0$ nm), the dose rate increases by, on average, a factor of 4.8, due to the enhanced scattering probability. This value agrees well with physical estimations and experiments as discussed below. We therefore use this as an upper limit estimation for the enhanced radiolysis effect in our kinetic reaction set.

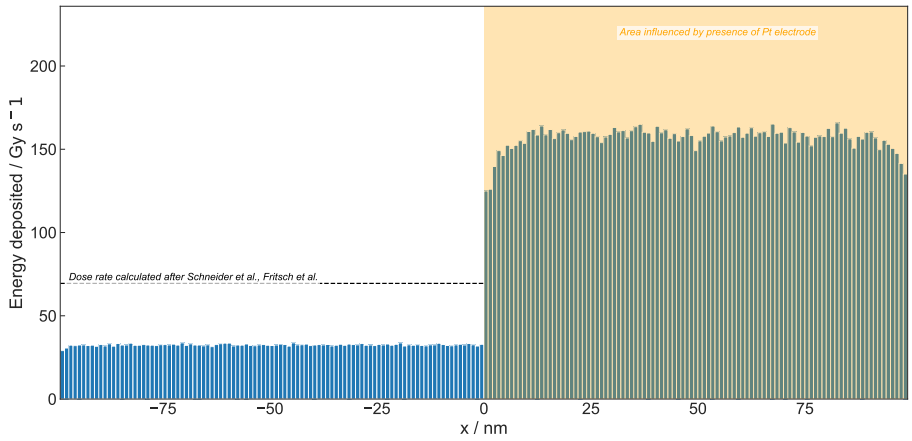

Figure SI 29: T*he energy deposited into the sample varies spatially along the cell. The dose rate is estimated from the energy change is calculated with the electron trajectories simulated with CASINO as described in the text. The dashed line indicates the value obtained via the established calculation of dose rate.*

Korpanty *et al*.[18] investigated whether gold particles (100 nm diameter) in solution increase radiolytic effects due to the increased scattering. They estimated the effect with a set of various models and measured the direct effect by electron energy loss spectrometry (EELS):

- Applying a linear model relying on the ratio of the stopping powers of the materials involved, which increased the effective dose rate by a factor of up to 1.7,
- applying a homogeneous model suggested that the effective dose can increase by a factor of up to 3,
- applying a heterogeneous model allowed for the estimation of a factor of dose rate increase up to 7,
- experimental measurement *via* EELS yielded a factor of dose rate increase of 1-1.25.

Gupta *et al*.[19] evaluates the special case of gold electrodes within the liquid cell in different scenarios of window material used. The increase of dose rate close to the solid-liquid interface can be estimated by a factor of roughly 2.5, while only to the first 5 nm of the liquid at the interface are directly affected. As gold and platinum have similar scattering cross sections, the results are comparable to our scenario.

While different approaches calculate or measure different proportionalities, the effective increase of dose rate near the solid-to-liquid interface consistently is a single-digit factor. An effect beyond an order of magnitude is therefore unlikely.

Radiolysis simulations

With kinetic reaction simulations[20] we can estimate the concentration of species in solution under the influence of radiolysis at the given conditions. The details on the implementation of mass transport are described in detail elsewhere[21], except for an extension of the reaction set by two reactions[22,23] (Table SI 5). These reactions were added to consider the radiolytic formation of H_2O_2, which can then be further catalyzed by the Pt surface, allowing for the

production of additional O_2, possibly contributing to Ag etching. The interested reader can find the rest of the reaction set in this reference.[21] The initial parameters used are listed in Table SI 3 and Table SI 4.

Table SI 3: Radical generation values (G-values) used in this work. The values were obtained from Schneider et al.[15] based on Hill and Smith[24]. The conversion to SI units can be found in Sun, Fritsch et al.[25].

Species	[molecules / 100 eV]	[10^{-7} mol/J]
$\mathbf{e_h^-}$	3.47	3.60
$\mathbf{H^+}$	4.42	4.58
$\mathbf{OH^-}$	0.95	0.98
$\mathbf{H_2O_2}$	0.47	0.49
H	1.00	1.04
OH	3.63	3.76
$\mathbf{HO_2}$	0.08	0.08
$\mathbf{H_2}$	0.17	0.18
$\mathbf{H_2O}$	-5.68	-5.89

Table SI 4: Initial concentration of different species used in this work. The initial concentration of all other species is 0 $mol \cdot L^{-1}$.

Species	**Initial concentration / $\mathbf{mol \cdot L^{-1}}$**
$\mathbf{H_2O}$	55.56
$\mathbf{H^+}$	$1 \cdot 10^{-7}$
$\mathbf{OH^-}$	$1 \cdot 10^{-7}$
$\mathbf{O_2}$	$2.55 \cdot 10^{-4}$
$\mathbf{Ag^+}$	$1 \cdot 10^{-2}$
$\mathbf{NO_3^-}$	$1 \cdot 10^{-2}$

The additional reactions are listed in Table SI 5.

Table SI 5: Additional reactions to the reaction set of silver (nitrate) with Ag-clusters as used in [16,21] Kinetic model for $AgNO_3$ aqueous solutions. Here, k denotes the respective rate constant with units of $mol^{-n+1}\ dm^{3(n-1)}\ s^{-1}$, where n is the reaction order.

	Reaction			k
1	H_2O_2	$\rightarrow$	2OH	$4.4 \cdot 10^{-9}$
2	HO_2^-	$\rightarrow$	O^- + OH	$1.0 \cdot 10^{-5}$

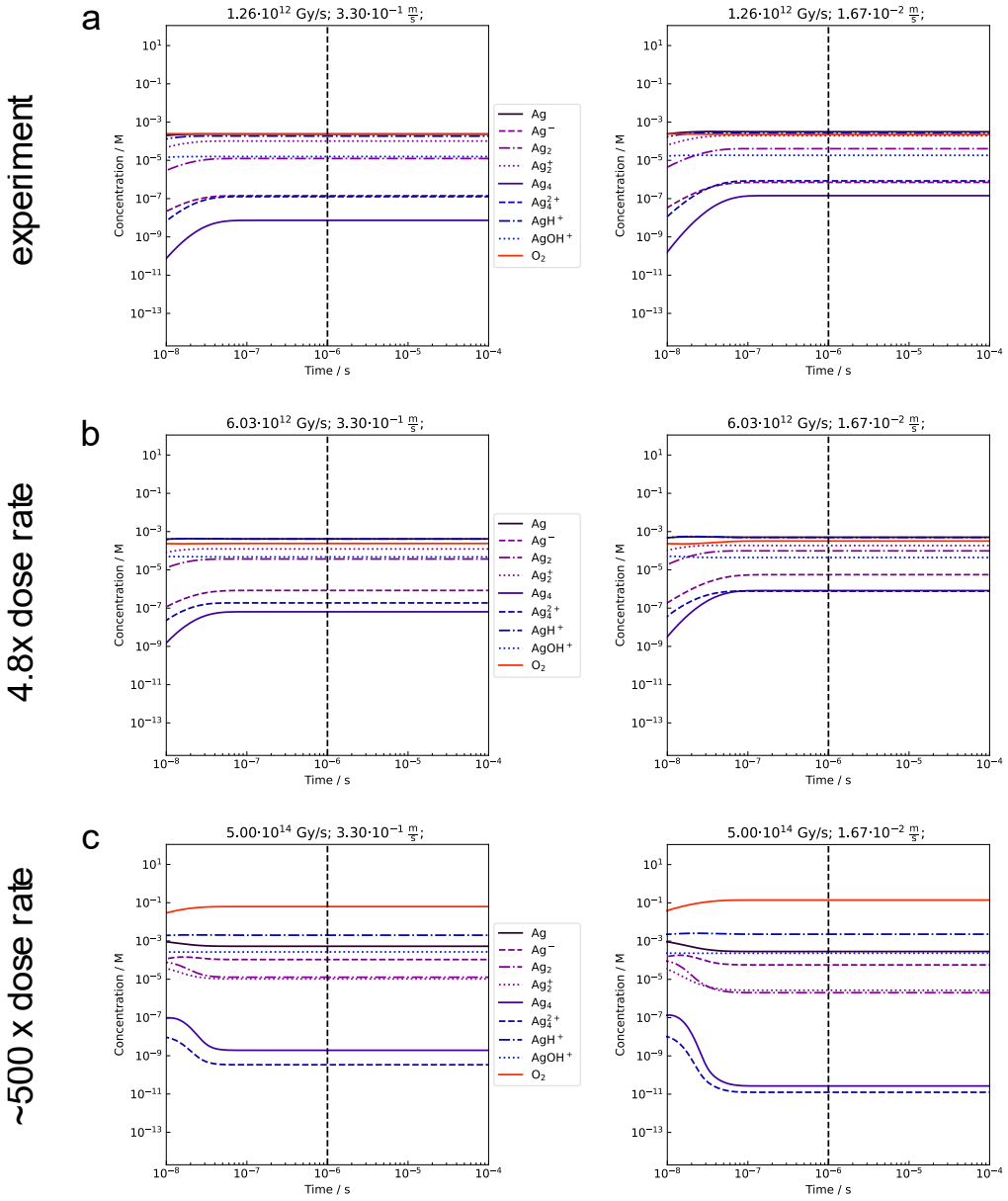

Figure SI 30: AuRaCh simulations at different dose rates(rows) and different flow velocities (columns) compute a concentration for the most relevant species (legend on top) for nucleation and particle growth over time.[25] The flow velocities represent upper and lower experimentally assessed flow velocity. The dashed black vertical line indicates the dwell time. The concentrations at this time are used for further evaluation.

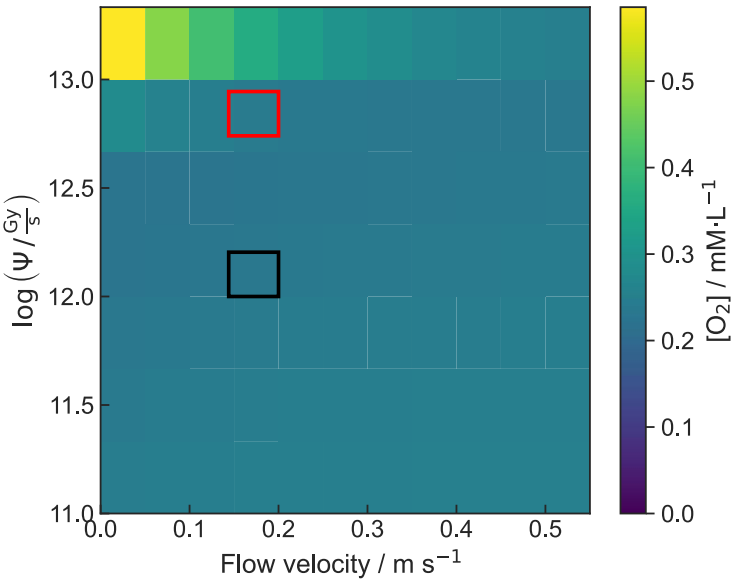

Figure SI 31: The ratio of the simulated concentrations of molecular oxygen at the end of the dwell time varies depending on dose rate Ψ and flow velocity. However, the ratio O_2 at the estimated dose rate and flow velocity in our experiments (black rectangle) is comparable to the situation at 4.8-times the dose rate (red rectangle).

As shown in Figure SI 31 the silver to oxygen ratio does not vary significantly around the dose rate and flow velocity parameters estimated from the experiments. Even a 4.8-fold increase in dose rate due to enhanced scattering (see CASINO-simulations) does not significantly alter the ratio. The silver concentration at the end of the dwell time is only significantly changed when the dose rate is altered by a factor of 500x the experimental parameters used here.

Furthermore, the addition of the H_2O_2 reaction shows that it does not cause a detrimental increase in O_2 concentration. This is also evident since its reaction rate of conversion is low, and little influence is expected based on radiolysis simulations.

Radiolysis influence is negligible for electrochemical effects

Growth and dissolution of particles not connected to the electrode are commonly observed and explainable *via* radiolysis of the electrolyte solution by the impinging electron beam. Radiolytic products, i.e., radicals and ions, react with the ions in solution to form (clusters of) elemental silver, which then nucleate and precipitate as particles.[20,25] Depending on the experimental conditions, such as flow rate, beam current, dwell time, and magnification (the

latter two in STEM only), radiolysis species are formed. In the case of Ag, the secondary radiolysis product O_2 is known to induce dissolution of elemental Ag structures. These processes have been simulated before.[21] The simulated trends have been validated experimentally, and here we utilize the same model to simulate the radiation chemistry for the herein applied conditions (Figure SI 30).

Furthermore, parts of the image far away from the electrode at the opposite side of the viewing window were analyzed to estimate overall radiolysis-induced growth and dissolution. This was then subtracted from the image signal to eliminate its influence. In most cases, these processes extend on a larger timescale and are much slower in comparison to the processes investigated correlating with electrochemistry (Figure SI 32). Lastly, the applied image analysis algorithm renders radiolytic effects negligible in the observed timescales.

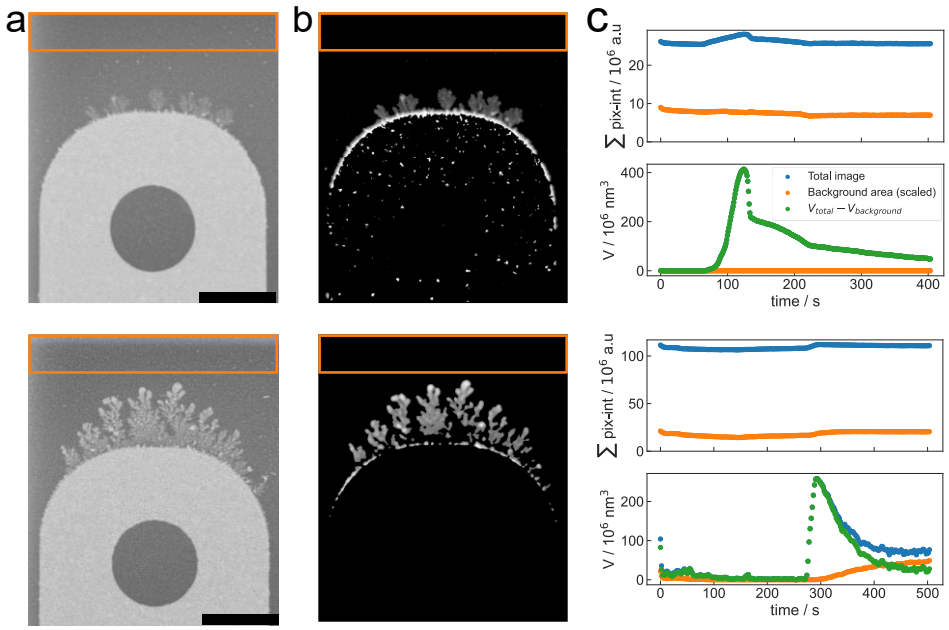

Figure SI 32:Radiolysis-driven evolution of silver particles far from the electrode (orange box and data points) is slow compared to the evolution driven by the electrochemical stimulus. Original image (a, scale bar 2 µm) and volume information (b) are shown for the data from Figure 2 and Figure 4, respectively. Summed pixel intensity (upper plot) are shown for the total image (blue) and the area considered background (orange, scaled to represent the whole image). The total estimated volume subtracted by the scaled background is shown in green in the lower plots.

The platinum electrode has a strong electron-scattering property, as discussed in the section on CASINO[12] simulations shown above (Figure SI 28 and Figure SI 29). However, we concluded the effective dose rates only increase by a one-digit factor. Consequently, the

effects on radiolysis products are minuscule. Furthermore, Gupta *et al.*[19] added the thought that, even when the dose rate (and therefore the production rate of reactive radiolytic species) is increased, the environment becomes more reductive. From this perspective, the electron-beam induced radiolysis is expected to rather reduce further silver ions from the solution, which contradicts our experimental observation.

Experimentally, the same fast dissolution of silver near the electrode is observed when the electron beam is blanked (Figure SI 11 - Figure SI 13). Therefore, the accelerated dissolution cannot be a beam-induced effect. This is also further supported by our SFC-ICP-MS experiments, where we see dissolution of Ag at OCP as well (Figure SI 27).

With all this, we acknowledged that radiolysis can be controlled by accurately monitoring a multitude of parameters. To name a few, it will depend on the concentration of different species, beam parameters such as dose rate and diameter, the thickness of the liquid film, flow speed of the liquid[21] which enable growth, dissolution, and morphological changes. From Figure SI 30, we theoretically achieved this neutral scenario. Still, in the presented experimental setup, some parameters evade the full control of the experimenter: the flow profile can change due to (electrochemically) growing or dissolving particles or form local concentration gradients of critical species such as Ag^+, which causes some visual radiolitic effects. This is the reason why we corrected for any radiolytic influence by looking into Ag particles present on the areas farthest away from the electrode within the observable window as indicators of the radiolytic effect. However, in all cases, radiolytic processes are much slower in comparison to electrochemically triggered events.

Inhomogeneities on the working electrode

The working electrode in the used configuration has 19 fingers. Two of them in the center of the hand are being imaged. However, *post mortem* analysis Figure SI 33 shows that the deposition happens inhomogeneously along the WE. Therefore, the material observable in the

window area might not be representative for the material deposited along the whole working electrode, which might explain deviations between image analysis and electrochemistry.

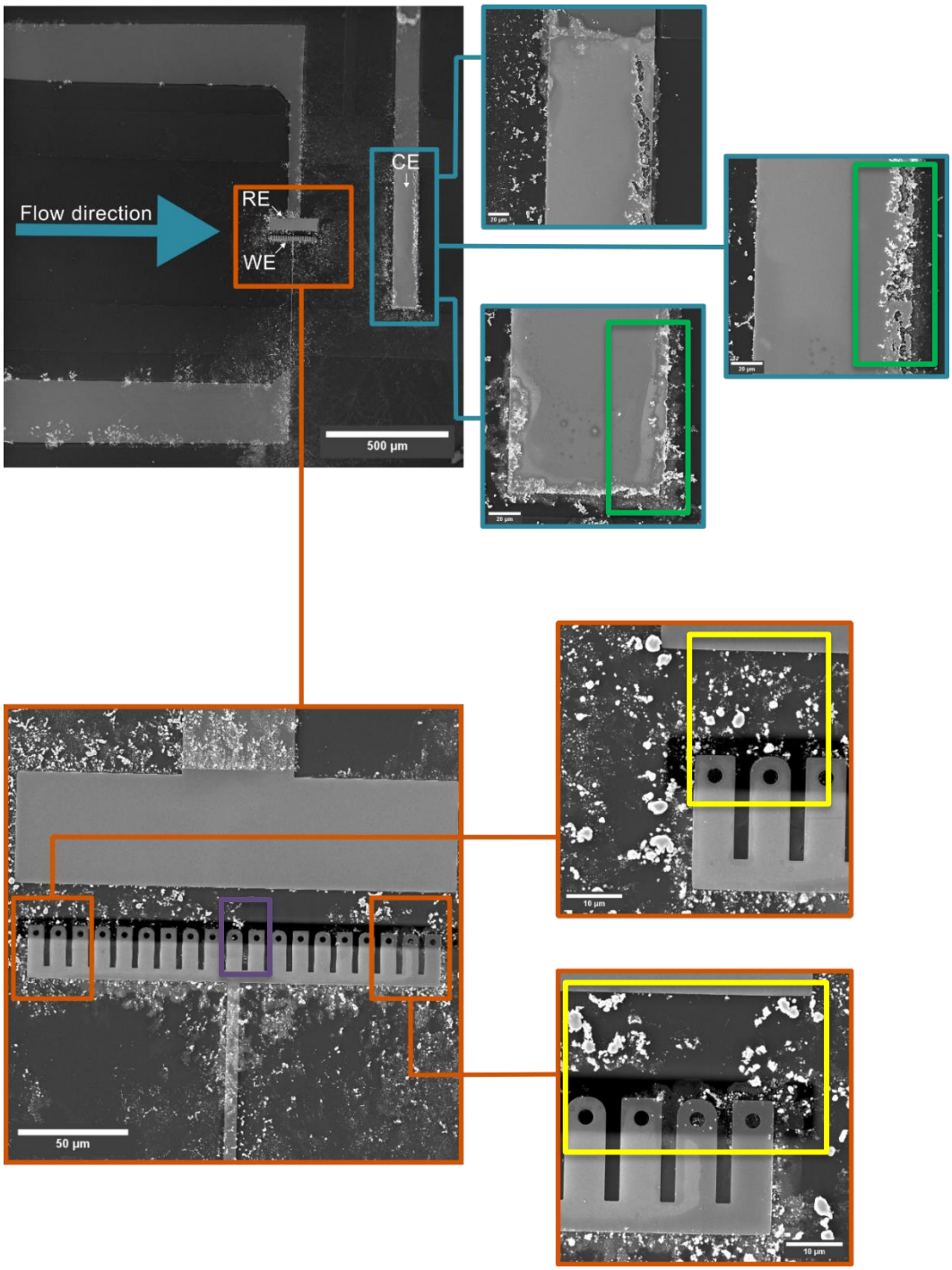

Figure SI 33: Overview of Nanochips for electrochemistry. The magnification images show a pronounced Pt degradation from the CE (degradation visible within the green rectangles). In the same way, the magnifications of the WE show the inhomogeneous behavior of the electrodeposition. However, more pronounced deposition occurs on the WE fingers at the edges. Besides, the yellow rectangle shows the presence of contact points between WE and RE. The purple rectangle shows the WE electrode fingers we imaged during the experiments.

References

1. Wedler, G. & Freund, H.-J. *Lehr- und Arbeitsbuch physikalische Chemie* (Wiley-VCH Verlag GmbH & Co. KGaA, Weinheim, Germany, 2018).
2. Bard, Allen J., Faulkner, Larry R., White, Henry S. *Electrochemical Methods Fundamentals and Applications* (John Wiley & Sons, 2001).
3. Inzelt, G. Crossing the bridge between thermodynamics and electrochemistry. From the potential of the cell reaction to the electrode potential. *ChemTexts* **1**; 10.1007/s40828-014-0002-9 (2015).
4. Sankara Papavinasam (ed.). *Electrochemical polarization techniques for corrosion monitoring.* 3 - Electrochemical polarization techniques for corrosion monitoring (Elsevier, 2008).
5. David Gray and Allen Cahill. Theoretical Analysis of Mixed Potentials. *Journal of The Electrochemical Society,* 443–447; 10.1149/1.2411894 (1969).
6. Lauf, P. *et al.* Be aware of the effect of electrode activation and morphology on its performance in gas diffusion electrode setups. *Journal of Power Sources* **623,** 235352; 10.1016/j.jpowsour.2024.235352 (2024).
7. Korber, A., Furcas, F. E., Pundir, M., Kammer, D. S. & Angst, U. M. PourPy - A python package to generate potential-pH diagrams. *JOSS* **9,** 6536; 10.21105/joss.06536 (2024).
8. M. Pourbaix. *Atlas of Electrochemical Equilibria in Aqueous Solutions* (NACE, 1974).
9. Linstrom, P. NIST Chemistry WebBook, NIST Standard Reference Database 69, 1997.
10. Einstein, A. Über die von der molekularkinetischen Theorie der Wärme geforderte Bewegung von in ruhenden Flüssigkeiten suspendierten Teilchen. *Annalen der Physik* **322,** 549–560; 10.1002/andp.19053220806 (1905).
11. Wei Xing, Geping Yin, Jiujun Zhang (ed.). *Rotating Electrode Methods and Oxygen Reduction Electrocatalysts.* Oxygen Solubility, Diffusion Coefficient, and Solution Viscosity (Elsevier, 2014).
12. Drouin, D. *et al.* CASINO V2.42: a fast and easy-to-use modeling tool for scanning electron microscopy and microanalysis users. *Scanning* **29,** 92–101; 10.1002/sca.20000 (2007).
13. Lowney, J. R. Monte Carlo simulation of scanning electron microscope signals for lithographic metrology. *Scanning* **18,** 301–306; 10.1002/sca.1996.4950180406 (1996).
14. LaVerne, J. A. & Pimblott, S. M. Electron Energy-Loss Distributions in Solid, Dry DNA. *Radiation Research* **141,** 208; 10.2307/3579049 (1995).
15. Schneider, N. M. *et al.* Electron–Water Interactions and Implications for Liquid Cell Electron Microscopy. *J. Phys. Chem. C* **118,** 22373–22382; 10.1021/jp507400n (2014).
16. Fritsch, B. *et al.* The Influence of Ionizing Radiation on Quantification for In Situ and Operando Liquid-Phase Electron Microscopy. *Adv Mater* **37,** e2415728; 10.1002/adma.202415728 (2025).
17. Castillo-Rico, L. R., Flores-Mancera, M. A. & Massillon-JL, G. Stopping power and CSDA range of electrons in liquid water, LiF, CaF2, and Al2O3 from the energy gap up to 433 keV. *Nuclear Instruments and Methods in Physics Research Section B: Beam Interactions with Materials and Atoms* **502,** 189–197; 10.1016/j.nimb.2021.07.002 (2021).

18. Korpanty, J., Parent, L. R. & Gianneschi, N. C. Enhancing and Mitigating Radiolytic Damage to Soft Matter in Aqueous Phase Liquid-Cell Transmission Electron Microscopy in the Presence of Gold Nanoparticle Sensitizers or Isopropanol Scavengers. *Nano letters* **21,** 1141–1149; 10.1021/acs.nanolett.0c04636 (2021).

19. Gupta, T., Schneider, N. M., Park, J. H., Steingart, D. & Ross, F. M. Spatially dependent dose rate in liquid cell transmission electron microscopy. *Nanoscale* **10,** 7702–7710; 10.1039/c8nr01935e (2018).

20. Fritsch, B. *et al.* Radiolysis-Driven Evolution of Gold Nanostructures - Model Verification by Scale Bridging In Situ Liquid-Phase Transmission Electron Microscopy and X-Ray Diffraction. *Advanced science (Weinheim, Baden-Wurttemberg, Germany)* **9,** e2202803; 10.1002/advs.202202803 (2022).

21. Körner, A., Fritsch, B., Morales, A. L., Malgaretti, P. & Hutzler, A. Panta Rhei - tuning silver nanostructure evolution with flow and radiolysis in liquid phase STEM. *Nano Today* **61,** 102575; 10.1016/j.nantod.2024.102575 (2025).

22. Serra-Maia, R., Rimstidt, J. D. & Michel, F. M. Kinetic Effect of Surface Chemisorbed Oxygen on Platinum-Catalyzed Hydrogen Peroxide Decomposition. *Catal Lett* **151,** 138–146; 10.1007/s10562-020-03280-2 (2021).

23. Elliot, A. & McCracken, D. R. Computer modelling of the radiolysis in an aqueous lithium salt blanket: Suppression of radiolysis by addition of hydrogen. *Fusion Engineering and Design* **13,** 21–27; 10.1016/0920-3796(90)90028-5 (1990).

24. Hill, M. A. & Smith, F. A. Calculation of initial and primary yields in the radiolysis of water. *Radiation Physics and Chemistry* **43,** 265–280; 10.1016/0969-806X(94)90190-2 (1994).

25. Sun, J. *et al.* Discovery of Molecular Intermediates and Nonclassical Nanoparticle Formation Mechanisms by Liquid Phase Electron Microscopy and Reaction Throughput Analysis. *Small Structures* **5**; 10.1002/sstr.202400146 (2024).